

ARTICLE

PD-1 regulates tumor-infiltrating CD8⁺ T cells in both a cell-intrinsic and a cell-extrinsic fashion

Kristen E. Pauken^{1,2*}, Samuel C. Markson^{1,2,3*}, Thomas S. Conway^{1,2}, Vikram R. Juneja^{1,2,4}, Osmaan Shahid^{1,2,5}, Kelly P. Burke^{1,2,6}, Jared H. Rowe^{1,2,7}, Thao H. Nguyen^{1,2}, Jenna L. Collier^{1,2}, Jaclyn M.L. Walsh^{1,2,3,8}, Megan E. Fung^{1,2}, Jacob M. Luber^{3,5,9}, Alison E. Ringel¹⁰, Jason M. Schenkel^{11,12}, Gordon J. Freeman⁶, Marcia C. Haigis¹⁰, Meromit Singer^{1,3,5}, and Arlene H. Sharpe^{1,2,3,12}

Although PD-1 inhibitors are FDA-approved for over 25 different cancers, the mechanisms contributing to response remain incompletely understood. To investigate how PD-1-deleted CD8⁺ T cells influence PD-1-expressing CD8⁺ T cells in the same tumor microenvironment, we developed an inducible PD-1 knockout (KO) model in which PD-1 is deleted on ~50% of cells. PD-1 deletion beginning at day 7 after implantation of MC38 tumor cells led to robust tumor control. Remarkably, PD-1-expressing CD8⁺ T cells in the tumor had increased functionality similar to PD-1 KO CD8⁺ T cells. Using single-cell RNA-seq and TCR-seq, we found that the major transcriptional changes following PD-1 deletion were shared by PD-1 KO and PD-1-expressing CD8⁺ T cells, although PD-1 KO clones preferentially expanded. These data suggest PD-1 inhibitors not only exert cell-intrinsic effects but also may promote increased T cell function through non-cell-autonomous mechanisms, which has important implications for design of PD-1-based cancer immunotherapies.

Introduction

Immunotherapy represents a major paradigm shift in cancer treatment, aiming to boost the immune response to malignant cells rather than directly targeting the cancer itself. Tumors hijack a number of immunosuppressive mechanisms to evade host immunity, including the programmed death (PD)-1 pathway (Sharma and Allison, 2015a; Sharpe and Pauken, 2018; Topalian et al., 2016; Vesely et al., 2022). PD-1 (CD279, encoded by the Pdcdl gene) is a co-inhibitory receptor (IR) expressed on all T cells during initial activation. PD-1 expression remains high and sustained during chronic infection and in many cancers due to persistent antigen stimulation. PD-1 is a key mediator of T cell dysfunction during chronic infection and cancer, as blockade of the pathway improves effector functions in exhausted CD8+ T cells (referred to as $T_{\rm EX}$) and causes a decrease in viral load or tumor burden (Sharma and Allison, 2015a; Sharpe and Pauken,

2018; Topalian et al., 2016; Vesely et al., 2022). Inhibitors of the PD-1 pathway have revolutionized clinical cancer care, and are now approved by the U.S. Food and Drug Administration for use in over 25 cancers (Pauken et al., 2021b; Ribas and Wolchok, 2018; Sharma and Allison, 2015b; Topalian et al., 2020; Vesely et al., 2022). Despite these promising results, most patients fail to show long-term clinical benefit, highlighting the need for a better mechanistic understanding of how PD-1 pathway blockade improves antitumor immunity.

Engagement of PD-1 by its ligands PD-L1 (B7-H1; CD274) or PD-L2 (B7-DC; CD273) induces inhibitory signals in T cells, countering the positive signals delivered through the T cell receptor (TCR) and CD28 and diminishing effector functions (Hui et al., 2017; Kamphorst et al., 2017; Latchman et al., 2001; Parry et al., 2005; Sharpe and Pauken, 2018; Yokosuka et al., 2012;

¹Department of Immunology, Blavatnik Institute, Harvard Medical School, Boston, MA, USA; ²Gene Lay Institute of Immunology and Inflammation, Brigham and Women's Hospital, Massachusetts General Hospital and Harvard Medical School, Boston, MA, USA; ³Broad Institute of MIT and Harvard, Cambridge, MA, USA; ⁴Harvard-MIT Division of Health Sciences and Technology, Cambridge, MA, USA; ⁵Department of Data Sciences, Dana-Farber Cancer Institute, Boston, MA, USA; ⁶Department of Medical Oncology, Dana-Farber Cancer Institute and Harvard Medical School, Boston, MA, USA; ⁷Division of Pediatric Oncology, Dana-Farber Cancer Institute, Boston, MA, USA; ⁸Division of Gastroenterology, Hepatology and Nutrition, Boston Children's Hospital, Harvard Medical School, Boston, MA, USA; ⁹Department of Biomedical Informatics, Harvard Medical School, Boston, MA, USA; ¹⁰Department of Cell Biology, Blavatnik Institute, Harvard Medical School, Boston, MA, USA; ¹¹Koch Institute for Integrative Cancer Research, Massachusetts Institute of Technology, Cambridge, MA, USA; ¹²Department of Pathology, Brigham and Women's Hospital, Boston, MA, USA.

*K.E. Pauken and S.C. Markson contributed equally to this paper. Correspondence to Arlene H. Sharpe: arlene_sharpe@hms.harvard.edu

K.E. Pauken's current affiliation is Department of Immunology, The University of Texas MD Anderson Cancer Center, Houston, TX, USA. V.R. Juneja's current affiliation is BioNTech US, Cambridge, MA, USA. J.M. Schenkel's current affiliation is Department of Laboratory Medicine, Department of Immunology, Department of Translational Molecular Pathology, The University of Texas MD Anderson Cancer Center, Houston, TX, USA. M. Singer's current affiliation is Guardant Health, Palo Alto, CA, USA. A.E. Ringel's current affiliation is Department of Biology, Massachusetts Institute of Technology (MIT), Cambridge, MA, USA. A.E. Ringel's current affiliation is Ragon Institute of Mass General, MIT, and Harvard, Cambridge, MA, USA. A.E. Ringel's current affiliation is Koch Institute for Integrative Cancer Research, Cambridge, MA, USA.

© 2025 Pauken et al. This article is distributed under the terms as described at https://rupress.org/pages/terms102024/.





Zinselmeyer et al., 2013). One mechanism by which PD-1 works is through direct cell-intrinsic inhibition of T cell signaling. Mechanistically, PD-1 ligation can (1) antagonize the TCR and CD28 through recruitment of phosphatases, (2) attenuate the PI3K/AKT/mTOR pathway, (3) modulate Ras signaling, and (4) induce BATF expression, culminating in changes that reduce T cell proliferation and effector functions (Patsoukis et al., 2020; Pauken and Wherry, 2015). Adoptive transfer studies of mixed wild-type (WT) and PD-1 knockout (KO) CD8+ T cells into mice followed by infection with acute lymphocytic choriomeningitis virus (LCMV), chronic LCMV, or acute influenza virus have further demonstrated a cell-intrinsic role of PD-1 in regulating CD8+ T cell functions (Kalia et al., 2021; Odorizzi et al., 2015; Pauken et al., 2020). In chronic LCMV infection, PD-1 KO CD8+ T cells showed increased expansion and effector potential early in infection but undergo more severe contraction and become more terminally exhausted than WT CD8+T cells (Odorizzi et al., 2015), providing mechanistic insight into how PD-1 can regulate CD8⁺ T_{FX} cells.

While these studies demonstrated a clear cell-intrinsic role of PD-1 in regulating CD8+ T cell functions, whether the protective anticancer effects that occur following PD-1 inhibition are solely dependent on cell-intrinsic consequences remains unclear. PD-1 deletion or blockade also may exert cell-extrinsic effects, i.e., affecting WT cells proximal to cells with inhibited or deleted PD-1. It is well established that PD-1 blockade can result in enhanced CD8+ T cell functionality in the tumor microenvironment (TME) (Sharma and Allison, 2015a; Sharpe and Pauken, 2018; Topalian et al., 2016; Vesely et al., 2022), with production of effector molecules (e.g., IFNγ, TNFα, and IL-2) that can have broad acting effects both locally and systemically, orchestrating a potent antipathogen or antitumor state in some settings (Iijima and Iwasaki, 2014; Rosato et al., 2019; Schenkel et al., 2014). These effector molecules can impact a number of different cell types, fundamentally changing the response of the entire tissue microenvironment (Iijima and Iwasaki, 2014; Rosato et al., 2019; Schenkel et al., 2014). Clinically, patients who respond better to checkpoint blockade (either PD-1 or CTLA-4 inhibitors) often show increased evidence of IFNy responses in the TME and tumor clearance, and defects in IFNγ signaling can be associated with poor clinical outcomes (Ayers et al., 2017; Gao et al., 2016; Gocher et al., 2022; Grasso et al., 2020; Shin et al., 2017; Zaretsky et al., 2016). Consequently, there is significant potential for loss of PD-1 signaling to exert cell-extrinsic effects that contribute to productive antitumor immunity. These effects could be additive or synergistic with the cell-intrinsic changes downstream of PD-1.

In this study, we sought to determine whether cell-extrinsic consequences of PD-1 loss contribute to the improved antitumor CD8 $^+$ T cell responses observed following PD-1 deletion. We developed a mouse model where PD-1 could be inducibly deleted on \sim 50% of the CD8 $^+$ T cells (referred to as inducible PD-1^{del.} mice), allowing us to interrogate cell-intrinsic versus cell-extrinsic effects of PD-1 deletion by comparing CD8 $^+$ tumor-infiltrating lymphocytes (TILs) that deleted PD-1 (referred to as PD-1^{KO}) with CD8 $^+$ T cells expressing high levels of PD-1 (referred to as PD-1^{Hi}) in the same TME in a polyclonal T cell

repertoire. We used the MC38 colon adenocarcinoma tumor model for these studies, since MC38 tumors subcutaneously implanted in the flank are highly responsive to PD-1 immunotherapy as a single agent (Juneja et al., 2017; Woo et al., 2012). Using single-cell RNA sequencing (scRNA-seq) and scTCR-seq, we found that the major unique cell-intrinsic change following PD-1 deletion in this model was increased T cell clonal expansion. Remarkably, PD-1^{Hi} and PD-1^{KO} CD8+ TILs in the same TME showed similar transcriptional and functional changes, indicating that cell-extrinsic changes following PD-1 deletion can substantially reshape the antitumor response to improve functionality of CD8+T cells still expressing PD-1. Both PD-1Hi and PD-1^{KO} CD8⁺ TILs in the inducible PD-1^{del.} mouse showed increased enrichment for transcriptional signatures associated with more terminal exhaustion compared with PD-1Hi CD8+ TILs in WT control mice, suggesting that a cell-intrinsic loss of PD-1 signals is not required to promote transition to the terminally exhausted state. These data suggest that inhibition or deletion of PD-1 can have a broader impact than previously appreciated by inducing a more potent antitumor state that feeds back onto PD-1expressing T cells to improve their function.

Results

PD-1 deletion selectively on CD8* T cells is sufficient to promote antitumor immunity against MC38 tumors

To interrogate mechanisms by which loss of PD-1 promotes protective antitumor immune responses, we used the MC38 mouse colon adenocarcinoma tumor model because MC38 tumors are highly sensitive to PD-1 blockade with anti-PD-1 or anti-PD-L1, and rapidly controlled in germline PD-1 KO mice when implanted subcutaneously in the flank (Juneja et al., 2017; Raghavan et al., 2021; Woo et al., 2012). We first determined whether selective deletion of PD-1 only in CD8+ T cells was sufficient for the protective antitumor effects observed in germline PD-1 KO mice (Juneja et al., 2017). We bred mice containing a loxP-flanked Pdcd1 allele (termed PD-1f/f) (Tan et al., 2021) to mice expressing Cre recombinase under the control of a CD8-specific promoter (termed E8i-Cre) (Maekawa et al., 2008) to permanently delete PD-1 on CD8+ T cells (referred to as CD8-Cre^{POS} PD-1^{f/f}, Fig. 1 A). CD8⁺ TILs in MC38 tumors of CD8-Cre^{POS} PD-1^{f/f} mice lacked PD-1 protein expression, while the frequencies of PD-1+ CD4+ Foxp3+ and CD4+ Foxp3- cells were comparable to levels observed in CD8-Cre^{NEG} PD-1^{f/f} control mice (Fig. 1, B and C). In contrast, the PD-1 protein was absent on both CD8+ and CD4+ TIL (both Foxp3+ and Foxp3-) in the germline PD-1^{KO} (referred to as global PD-1^{KO}) where PD-1 is deleted on all cells (Fig. 1, B and C).

We next compared tumor growth to assess the impact on the antitumor immune response. As expected, CD8-Cre^{NEG} PD-1^{f/f} mice failed to control MC38 tumors (Fig. 1 D). Consistent with our previous work (Juneja et al., 2017), global PD-1^{KO} rapidly controlled MC38 tumors, with 100% of the mice routinely clearing their tumors (Fig. 1 D). CD8-Cre^{POS} PD-1^{f/f} mice, which only lacked PD-1 on CD8+ T cells, also showed robust tumor control compared with CD8-Cre^{NEG} PD-1^{f/f} mice, with 70% of mice clearing tumors (Fig. 1 D). These data suggest that selective



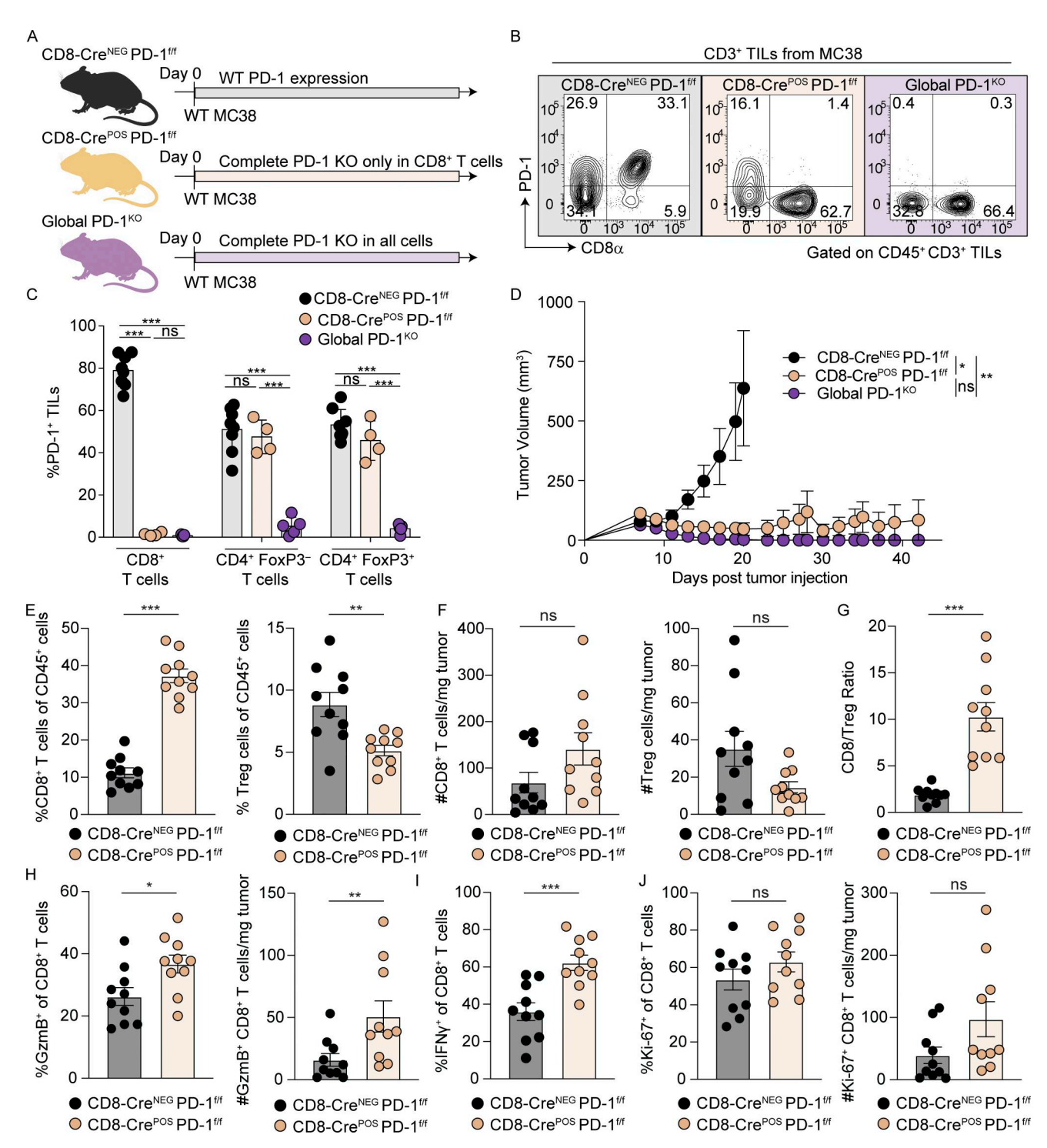


Figure 1. **PD-1 expressed by CD8* T cells is largely sufficient for protective antitumor immunity against subcutaneous MC38. (A)** Schematic for germline deletion of PD-1 selectively on CD8* T cells (using the E8i-Cre^{POS} PD-1^{f/f} mouse) or on all cells (using the global PD-1^{KO} mouse). E8i-Cre^{NEG} PD-1^{f/f} mice were included as a WT control. Schematic created using https://BioRender.com. **(B)** Representative flow cytometry contour plots showing PD-1 (y axis) versus CD8 α (x axis) expression. Plots are gated on CD45* CD3* TILs at day 11 after implantation of MC38 tumor cells into WT (E8i-Cre^{NEG} PD-1^{f/f}), CD8 conditional PD-1 KO (E8i-Cre^{POS} PD-1^{f/f}), and PD-1 germline KO (global PD-1^{KO}). **(C)** Quantification of the flow cytometry in B, showing the frequency PD-1* of CD8* T cells, CD4* FoxP3* T cells (conventional CD4* T cells), and CD4* Foxp3* (Tregs) from MC38 tumors at day 11 after tumor cell implantation. Data shown are from one representative experiment with n = 4-8 mice per group. Data are representative of two independent experiments with at least three mice per group comparing all three mouse strains (CD8-Cre^{NEG} PD-1^{f/f}, CD8-Cre^{POS} PD-1^{f/f}, and global PD-1^{KO}), and an additional four independent experiments comparing CD8-Cre^{NEG} PD-1^{f/f} mice. A two-way ANOVA was performed with Tukey's multiple comparisons test. A P value for all comparisons is marked with "****," P < 0.0001. For comparisons labeled as not significant (ns): CD8* T cells, P = 0.9906; CD4* FoxP3* T cells, P = 0.6966; CD4* FoxP3* T cells, P = 0.2088. **(D)** Tumor growth curves in WT control (E8i-Cre^{NEG} PD-1^{f/f}), CD8 conditional PD-1 KO (E8i-Cre^{POS} PD-1^{f/f}), and PD-1 germline KO (global PD-1^{KO}) mice, showing tumor volume (mm³) over time (days) after implantation of MC38 tumor cells subcutaneously in the flank. Data shown are from one representative experiment



with n = 5-10 mice per group. Data are representative of three independent experiments with at least four mice per group. A one-way ANOVA (Kruskal–Wallis test) with Dunn's multiple comparisons was performed for the day 23 time point (endpoint for CD8-Cre^{NEG} PD-1^{f/f}). CD8-Cre^{NEG} PD-1^{f/f} versus CD8-Cre^{POS} PD-1^{f/f}, P = 0.0136*; CD8-Cre^{POS} PD-1^{f/f} versus global PD-1^{KO}, P = 0.8391; CD8-Cre^{NEG} PD-1^{f/f} versus global PD-1^{KO}, P = 0.0021**. **(E-J)** Analysis of TIL from MC38 tumors at days 11–13 after tumor cell implantation in CD8-Cre^{NEG} PD-1^{f/f} and CD8-Cre^{POS} PD-1^{f/f} mice using flow cytometry. **(E)** Frequency of CD8+ T cells (left, P < 0.0001***) and Treg cells (right, P = 0.0027**) of total CD45+ cells. **(F)** Number of CD8+ T cells (left, not significant, P = 0.0630) and Treg cells (right, not significant, P = 0.0514) per milligram of tumor. **(G)** Ratio of CD8+ T cells to Treg cells in the tumor, P < 0.0001***. **(H)** Frequency (left, P = 0.0190*) and number per milligram (right, P = 0.0089**) of CD8+ T cells expressing granzyme B protein (abbreviated "GzmB"). **(I)** Frequency of IFNy-producing CD8+ T cells following ex vivo stimulation with PMA and ionomycin, P = 0.0006***. **(J)** Frequency (left, not significant, P = 0.2351) and number per milligram (right, not significant, P = 0.6842) of CD8+ T cells expressing Ki-67 protein. Data shown in E-J are from two experiments combined for a total of n = 10 CD8-Cre^{NEG} PD-1^{f/f} and n = 10 CD8-Cre^{POS} PD-1^{f/f}. For E-J, significance was determined using an unpaired t test if both groups were normally distributed, or the Mann–Whitney test if both groups were not normally distributed. Representative of 2-7 total experiments with at least three mice per group per experiment.

loss of PD-1 on CD8+ T cells is largely sufficient to promote antitumor immunity against MC38 tumors. Consistent with the improved tumor control, there were an increase in the frequency of CD8+ T cells as a percentage of CD45+ cells, and a trend toward increased numbers of CD8+ T cells per milligram of tumor (Fig. 1, E and F). There was a concomitant decrease in the frequency of regulatory T (Treg) cells of CD45+ cells, and a trend toward decreased numbers of Treg per milligram of tumor (Fig. 1, E and F). Importantly, the CD8/Treg ratio was increased in CD8-Cre POS PD- $1^{f/f}$ mice compared with CD8-Cre NEG PD- $1^{f/f}$ control mice, suggesting a shift toward a more proinflammatory TME (Fig. 1 G). Moreover, there was an increased frequency and number per milligram of tumor of granzyme B-expressing CD8+ TILs in CD8-Cre POS PD-1 $^{f/f}$ mice compared with CD8-Cre NEG PD-1^{f/f} control mice (Fig. 1 H), as well as an increase in IFN γ producing CD8+ TILs (Fig. 1 I). It should be noted that there was no difference in the frequency of Ki-67+ CD8+ TILs between groups, though there was a trend toward increased numbers of Ki-67⁺ CD8⁺ TILs in the CD8-Cre^{POS} PD-1^{f/f} mice that did not reach significance (Fig. 1 J). Collectively, these data demonstrate that PD-1 deletion on CD8+ T cells is sufficient for the protective effects following PD-1 loss in MC38 tumors and highlight the importance of understanding how PD-1 regulates this cell type.

Inducible deletion of PD-1 on about 50% of cells leads to robust tumor control, providing a means to analyze the cell-intrinsic versus cell-extrinsic effects of PD-1 deletion in the TME

We next asked whether the protective effects of PD-1 deletion in MC38 tumors were due to the ability of PD-1 to suppress T cell functions in a cell-autonomous manner, or whether loss of PD-1 signals could induce broader changes in the TME that could promote the functions of neighboring CD8⁺ T cells. To address this question, we developed an inducible PD-1 KO mouse model where the timing and extent of PD-1 deletion could be controlled. We bred PD-1f/f mice to CreERT2 mice, in which the Cre recombinase gene is fused to the estrogen receptor (CreERT2) under the control of the human ubiquitin promoter (Ruzankina et al., 2007), allowing inducible deletion of PD-1 on all cell types upon tamoxifen administration (Fig. 2 A) (UBC-CreERT2+ PD-1f/f mice, referred to as inducible PD-1^{del.} mice). This model has the advantage that the timing of deletion can be controlled (unlike a germline, noninducible PD-1 KO), allowing T cell development to progress normally, and deletion at therapeutically relevant time points. This model mimics the use of PD-1 inhibitors, where

antibodies are given systemically and can block any cell actively expressing PD-1 (Raghavan et al., 2021).

Five doses of tamoxifen resulted in about 40% deletion of PD-1 on splenic CD8+ T cells, with upregulation of the PD-1 protein in about 60% of splenic CD8+ T cells from inducible PD-1^{del.} mice after in vitro stimulation with anti-CD3 and anti-CD28 (Fig. 2 B). In contrast, in UBC-CreERT2⁻ PD-1^{f/f} control mice (referred to as WT control), about 95% of splenic CD8+T cells upregulated PD-1 following in vitro stimulation (Fig. 2 B). In MC38 tumors, about 85% of CD8+ TILs express the PD-1 protein in WT control mice, whereas in inducible PD-1^{del.} mice, only about 40% of CD8+ TILs express the PD-1 protein (Fig. 2, C and D). There also was a 50-60% reduction in the frequency of PD-1+ cells in the CD4+ TIL compartment on both Foxp3⁺ and Foxp3⁻ CD4⁺ T cells (Fig. 2 D), as expected due to the ubiquitous expression of CreERT2. Importantly, the PD-1Hi CD8+ TILs in inducible PD-1del. mice showed similar levels of PD-1 phosphorylation on the immune receptor tyrosine-based switch motif (ITSM) motif (see Materials and methods) (Bu et al., 2021) as CD8+ TILs in WT control mice, indicating that PD-1Hi CD8+ TILs in inducible PD-1del. mice can signal through PD-1 (Fig. 2 E).

We also examined the impact of PD-1 deletion on tumor growth using this 5-dose tamoxifen regimen that led to PD-1 deletion in ~50% of cells. Administration of tamoxifen prior to, early (days 0-5), or later after tumor implantation (days 7-11) resulted in robust tumor control in inducible PD-1^{del.} mice, while WT control mice failed to control tumors (Fig. 2, F-H). Consistent with superior tumor growth control, the CD8/Treg ratio increased in the inducible PD-1 $^{\rm del.}$ compared with the WT control mice following deletion of PD-1 from days 7 to 11 (Fig. 2 I), suggesting that PD-1 deletion resulted in improved antitumor immunity in this setting. Thus, the inducible PD-1^{del.} mouse provides a model for analyzing the cell-intrinsic versus cellextrinsic effects of PD-1 deletion by comparing CD8+ TILs that have deleted PD-1 with PD-1-expressing CD8⁺ T cells that still express the PD-1 protein and can respond to PD-1 signals within the same TME.

Deletion of PD-1 induces a potent antitumor state in MC38 tumors associated with transcriptional signatures of IFN stimulation, effector functions, and exhaustion in CD8+ TILs

To examine how deletion of PD-1 in \sim 50% of cells affected the biology of CD8 $^+$ TILs in this setting of protective antitumor immunity, we implanted MC38 tumor cells, administered tamoxifen from days 7 to 11 to induce PD-1 deletion, and performed



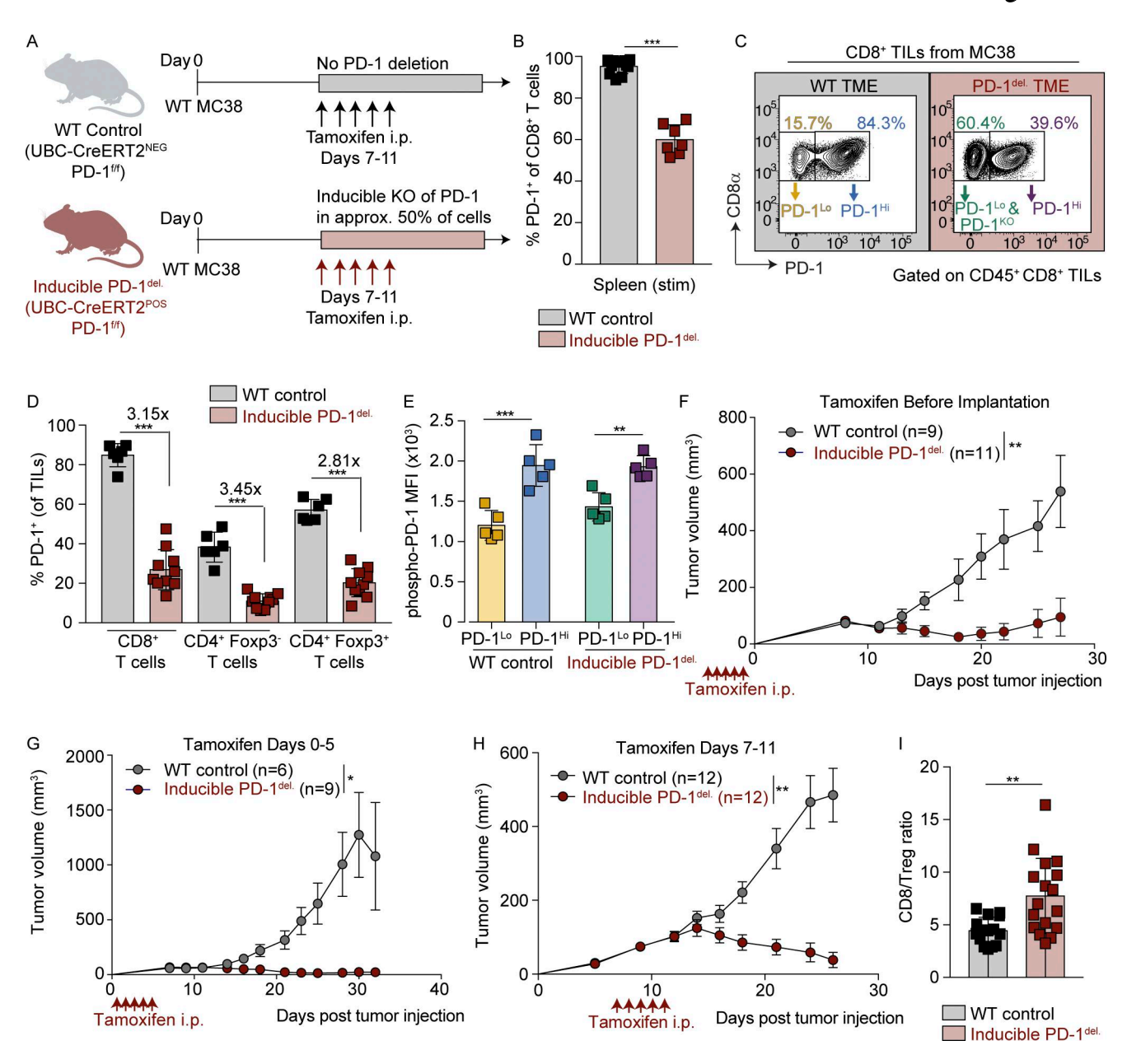


Figure 2. Development of an inducible PD-1 deletion model to study PD-1-sufficient and PD-1-deleted CD8* T cells in the same TME. (A) Schematic for inducible PD-1 deletion. Mice containing loxP-flanked Pdcd1 alleles (PD-1^{f/f}) and expressing either one copy of UBC-CreERT2 (UBC-CreERT2+ PD-1^{f/f}, referred to as "inducible PD-1^{del.}" mouse) or no copies of UBC-CreERT2 (UBC-CreERT2 PD-1^{f/f}, referred to as "WT control" mouse) received daily tamoxifen (1 mg/ mouse/day) i.p. from days 7 to 11 (unless otherwise indicated) after MC38 tumor cell implantation to delete exons 2-4 of Pdcd1. The schematic was created with https://BioRender.com. (B) Percentage of splenic CD8+ T cells expressing PD-1 protein following 24 h in vitro stimulation with anti-CD3 and anti-CD28. Data shown are one experiment with n = 11 WT control and n = 7 inducible PD-1^{del}. mice. Data are representative of three independent experiments with at least n = 3WT control and at least n = 5 inducible PD-1^{del.} per group. An unpaired t test was performed not assuming normal distribution (Mann-Whitney test), P < 0.0001***. (C) Representative flow cytometry contour plots showing PD-1(x axis) by CD8a expression (y axis) on CD8+ T cells in MC38 tumors harvested at day 17. Full gating strategy was based on size, singlets, live, CD45+, CD8+ cells. (D) Quantification of the frequency of CD8+ T cells, CD4+ Foxp3- T cells, and CD4+ Foxp3+ T cells expressing PD-1 in MC38 tumors in WT control mice versus inducible PD-1^{del}. mice shown in C. Data shown are one representative experiment with n = 6 WT control mice and n = 10 inducible PD-1^{del.} mice. Data are representative of five experiments with at least five mice per group. Normality was determined using the Shapiro-Wilk test, and significance was assessed using a one-way ANOVA with Tukey's multiple comparisons tests. Asterisks (***) indicate P < 0.0001 for each pairwise comparison indicated in this figure. (E) Quantification of the levels of PD-1 phosphorylation in CD8+ TILs in MC38 tumors at day 17 after tumor cell implantation. Phospho-PD-1 levels were determined using an antibody that specifically detects the phosphorylated ITSM motif of PD-1 by flow cytometry as described previously (Bu et al., 2021). Data shown are one experiment with n = 5 mice per group and representative of two independent experiments with three to five mice per group. A one-way ANOVA was performed with Tukey's multiple comparisons test. WT control PD-1^{Lo} versus PD-1^{Hi}, P < 0.0001***; inducible PD-1^{KO} PD-1^{Lo} versus PD-1^{Hi}, P = 0.0045**. **(F-H)** Tumor growth curves showing tumor volume (mm³) over time (days) after subcutaneous injection of MC38 tumor cells. Arrows indicate the timing of tamoxifen administration to induce PD-1 deletion. Tamoxifen was administered (F) prior to tumor cell injection (n = 9 WT and n = 11 inducible PD-1^{del.}), (G) at days 0-5 after tumor cell injection (n = 6 WT and n = 9 inducible PD-1^{del.}), or (H) days 7-11 after tumor cell injection (n = 12 per genotype). Data in F-H are from one representative experiment each. F and G are each representative of two independent



experiments with at least n = 6 per group. H is representative of three experiments with at least n = 3 WT control and at least n = 5 inducible PD-1^{del.} mice per group. Significance was assessed using the Mann–Whitney unpaired t test at the endpoint for the WT control. **(F)** Day 27, P = 0.0019**. **(G)** Day 32, P = 0.0182*. **(H)** Day 31, P = 0.0011**. **(I)** CD8/Treg ratio in MC38 tumors at day 17 after tumor cell implantation. Data shown are from two experiments combined with n = 15 (WT control) and n = 17 (inducible PD-1^{del.}). Data are representative of three independent experiments with at least five mice per group. Significance was assessed using an unpaired t test, P = 0.0020**. In A–I, WT control refers to UBC-CreERT2- PD-1^{f/f} mice, and inducible PD-1^{del.} refers to UBC-CreERT2+ PD-1^{f/f} mice.

droplet-based (using 10X Genomics) scRNA-seq with paired TCR-seq (scTCR-seq) at days 16–17. For all cells, we also determined PD-1 protein status (e.g., PD-1^{Hi} or PD-1^{Lo}) by either FACS-based sorting based on detection of PD-1 using a fluorescently conjugated antibody prior to 10X or performing Cellular indexing of transcriptomes and epitopes by sequencing (CITE-seq) to detect the PD-1 protein computationally (Fig. S1, A–F; see Materials and methods). We chose this timing for PD-1 deletion to recapitulate the timing associated with the response to therapeutic blockade using monoclonal antibodies (Juneja et al., 2017).

We first determined how loss of PD-1 impacted the global CD8+ TIL population regardless of the PD-1 protein status by comparing total CD8+ TILs in inducible PD-1^{del.} mice with WT control mice (Fig. 3 A). We used Leiden clustering to broadly characterize the differences in CD8+ TILs between these two genotypes (n = 15,729 cells). Previous work established that MC38 tumors contain CD8+ TILs with diverse transcriptional phenotypes including several exhausted-like subpopulations (Bhatt et al., 2021; Pauken et al., 2021a; Wei et al., 2017). In our dataset, we identified eight major transcriptionally defined clusters, which were manually annotated for functional association based on significantly upregulated genes per cluster, distribution of key lineage-defining markers, enrichment for key signatures from the literature (e.g., cell cycle, response to IFN, exhaustion), and the co-expression of multiple IRs (see Materials and methods, Fig. 3 B; Fig. S2, A-D; and Tables S1 and S2). These clusters included transcriptional profiles associated with IFNstimulated T_{EX} (Cluster 0 including Isg15, Ifit1, Bst2, Mx1, Stat1, Usp18, and Cxcr6 and Gzmk), quiescent/progenitor-like T cells (Cluster 1 including Klf2, Tcf7, Bcl2, Sell, and Lef1), "immunesuppressed"/glycolytic T_{EX} cells (Cluster 2 including Tnfrsf18, Tnfrsf9, Bhlhe40, Ccr7, Ccr8, Nrp1, and Hifla, which have been associated with an immune-suppressed phenotype in tumors [Nelson et al., 2019; Schietinger et al., 2012; Watkins et al., 2021; Waugh et al., 2016, and Gapdh, Enol, Aldoa, and Ldha, which have been associated with glycolysis), terminally exhausted-like T_{EX} cells (Cluster 3 including Lag3, Havcr2, Prf1, Gzmb, Tigit, Ccl4, and Cxcr6), intermediate exhausted-like TEX cells (Cluster 4 including transcripts associated with ribosomal proteins [Rps/Rpl genes], Pdcd1, Bhlhe40, Tigit, Nr4a2, Irf8), cycling T cells (Cluster 5 including Tubb5, Cdkn3, Hmgb1, Kif23, Top2a, and Mki67), cytotoxic T_{EX} (Cluster 6 including Prfl, Gzmc, Gzme, Gzmd, Gzmb, and Gzmf), and an effector-like TEX population (Cluster 8 including Xcl1, Ccl3, Tnfsf14, Ccl4, Ccl1, Cd160, and Ifnq) (Fig. 3 B, Fig. S2 A, and Table S1). We also observed a population that appeared to contain non-T cells (Cluster 7 including Cd14, Cd68, Csf1r, Adgrel), which was likely due to a low level of contamination during sorting, and we excluded this cluster from downstream analyses that were focused on CD8+ TILs.

We next examined the distribution of CD8+ TILs from WT control versus inducible PD-1^{del.} mice across these transcriptional clusters (Fig. 3, C and D). CD8+ TILs from the inducible PD-1^{del.} mice occupied largely distinct areas of the Uniform Manifold Approximation and Projection (UMAP) compared with CD8+ TILs from WT control mice (Fig. 3 C). Consistent with this observation, principal component analysis (PCA) revealed the second PC (PC2) to clearly differentiate between CD8+ TILs from the inducible PD-1^{del.} and WT control (variance explained by PC1 = 2.197323% and PC2 = 1.159362%, Cohen's D effect size for PC1 = 0.082 and PC2 = 1.691, Fig. S3 A), indicating a substantial difference in the transcriptional landscape between inducible PD-1^{del.} and WT control mice. Quantification of each genotype across the clusters showed that Cluster 2 (immune-suppressed/ glycolytic T_{EX}) was the most prominent cluster in CD8⁺ TILs from WT control mice (45.99% of CD8+ TILs), while Cluster 3 (T_{EX} , terminal) was the most prominent cluster in CD8+ TILs from inducible PD-1^{del.} mice (43.73% of CD8+ TILs) (Fig. 3 D and Fig. S3 B). Between genotypes, CD8+ TILs from the inducible PD- $1^{\text{del.}}$ showed significantly enriched Cluster 3 (T_{EX} , terminal, P = 0, Fisher's exact test), Cluster 0 (IFN-stimulated T_{EX} , Fisher's exact test, P = 1.36 × 10⁻³⁹), and Cluster 4 (T_{EX} , intermediate, Fisher's exact test, $P = 3.26 \times 10^{-11}$) compared with WT control, while the WT control showed a significant increase in Cluster 2 (immunesuppressed/glycolytic T_{EX} , $P = 5.36 \times 10^{-282}$, Fisher's exact test), Cluster 1 (quiescent/Progenitor-like T cells, $P = 1.42 \times 10^{-4}$), and Cluster 5 (cycling T cells, Fisher's exact test, $P = 7.31 \times 10^{-3}$) (Fig. S3 B). These results were consistent across individual mice (Fig. S3 B). In accordance with this finding, differential gene expression analysis showed that CD8+ TILs from inducible PD-1^{del.} mice had elevated levels of cytotoxic and/or effector molecules, IRs, and signs of IFN stimulation, including Gzmb, Gzmk, Havcr2, Icos, Ccl4, Ccl5, Stat1, Bst2, and Usp18 (Table S3).

We next performed two types of analyses to assess pathways and transcriptional modules that were differentially expressed following PD-1 deletion. First, pathway analysis using Gene Set Enrichment Analysis (GSEA) showed elevated response to IFNα, IFNγ, and inflammation in CD8+ TILs from inducible PD-1^{del.} mice compared with WT control mice (Fig. S3 C and Table S4). Second, dissection of the multi-layered transcriptional programs present in the single-cell data using a type of topic modeling known as latent Dirichlet allocation (LDA) (Bielecki et al., 2021; Dev et al., 2017; Pritchard et al., 2000) also showed gene modules (called topics) associated with IFN stimulation/exhaustion, cytotoxicity and/or effector functions, and IRs elevated in CD8+ TILs from inducible PD-1^{del.} mice (Fig. 3 E, Fig. S3 D, and Table S5). Conversely, topics associated with quiescence and glycolytic metabolism were preferentially enriched in CD8+ TILs from WT control mice (Fig. 3 E, Fig. S3 D, and Table S5). Collectively, these



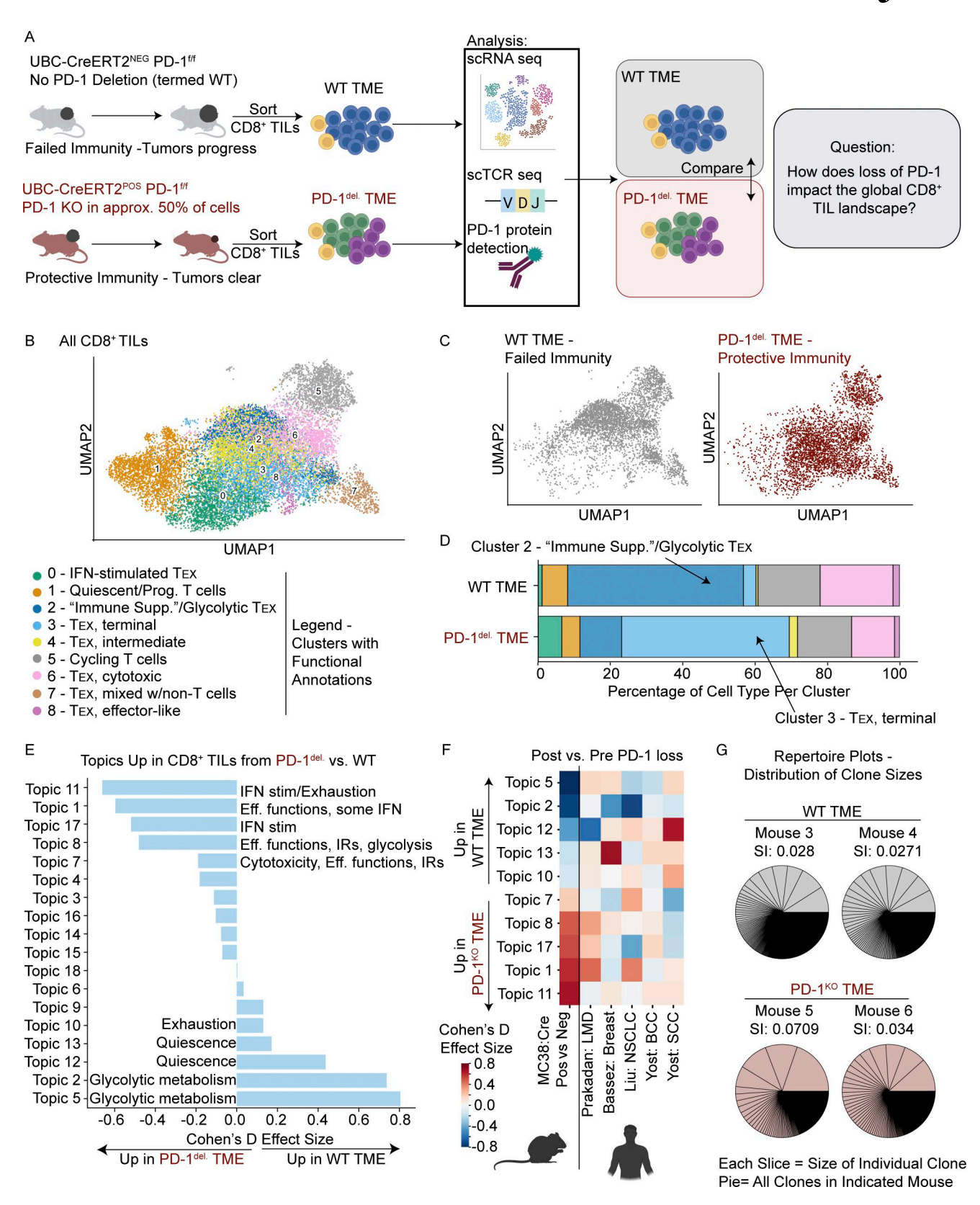


Figure 3. Protective antitumor immunity following genetic deletion of PD-1 is associated with transcriptional signatures of IFN stimulation, effector activity, and terminal exhaustion in CD8⁺ TILs in MC38 tumors. (A) Schematic of study design for interrogating mechanisms by which PD-1 loss promotes the development of protective immunity in CD8⁺ TILs in MC38 tumors, and for determining which changes are dependent on a cell-intrinsic loss of PD-1 versus cell-extrinsic consequences of PD-1 loss (e.g., changes in function in CD8⁺ TILs still expressing PD-1). The data in this figure compare total CD8⁺ TILs in inducible PD-1^{del.} mice (UBC-CreERT2⁺ PD-1^{f/f}) versus WT control mice (UBC-CreERT2⁻ PD-1^{f/f}) to define the impact of PD-1 deletion on the global CD8⁺ TIL population. (B) Clustering and UMAP visualization of CD8⁺ T cells (n = 15,729 cells) sorted from MC38 tumors from inducible PD-1^{del.} versus WT control mice



at days 16-17 after tumor implantation. Colors denote transcriptional clusters, labeled with functional annotations (see Materials and methods). A full list of upregulated genes per cluster can be found in Table S1. (C) UMAP visualization of CD8+ TILs from WT (n = 4,394 cells) versus inducible PD-1^{del.} mice (n = 3,785 cells). (D) Stacked bar plots showing the frequency of each population belonging to each functional cluster. The legend for the colors used in the bars is shared with the legend for the clusters in B. Cluster 7 was excluded from the bar plot since it likely contained non-T cells. Clusters are indicated in order from left to right, with Cluster 0 being the left-most cluster, and Cluster 8 being the right-most cluster. P values and φ coefficients showing the enrichment of cells across all clusters between the WT TME and inducible PD-1^{del.} TME can be found in Fig. S3 B. (E) Bar plot showing the enrichment of different topics in CD8+ TILs from WT control versus inducible PD-1^{del}. mice. The functional annotations for the top five ranked topics in each direction are indicated. A full list of topics and top 50 genes by weight in each topic can be found in Table S5. (F) Heat map showing the Cohen's D effect size of the top 5 differentially enriched topics in each direction in the MC38 dataset (up in CD8+ TILs from WT control mice, and up in CD8+ TILs from inducible PD-1^{del.} mice), and the enrichment of these topics in patient cohorts where scRNA-seq data were available on CD8+ TILs pre- and postcheckpoint blockade (either anti-PD-1 or anti-PD-1 plus anti-CTLA-4) (Bassez et al., 2021; Liu et al., 2022; Prakadan et al., 2021; Yost et al., 2019). (G) Pie chart showing the distribution of clone sizes in CD8+ TILs from WT control versus inducible PD-1^{del.} mice. Each pie represents data from an individual mouse. Also indicated is the Simpson Index (abbreviated as "SI" in the figure) for each sample. For analyses in B, shown are cells from two independent experiments (Exp 1+ Exp 2). For analyses in C-G, shown are cells from one independent experiment (Exp 2) where total CD8+ TILs were sorted regardless of PD-1 protein status in order to define the broad differences between CD8+ TILs in inducible PD-1^{del.} versus WT control mice, representing n = 2 mice per genotype. "WT TME" refers to CD8+ TILs that were isolated from WT control (UBC-CreERT2- PD-1ft) mice, and "PD-1del. TME" refers to CD8+ TILs that were isolated from inducible PD-1del. (UBC-CreERT2+ PD-1ft) mice. Schematics/images in A and F were created with https://BioRender.com. Abbreviations, Supp.: Suppressed, Prog.: Progenitor-like, TEX: T exhausted cell, Eff. function: Effector functions, LMD: leptomemingeal disease, Breast: breast cancer, NSCLC: non-small cell lung cancer, BCC: basal cell carcinoma, SCC: squamous cell carcinoma.

data suggest that changes in the IFN response and effector functions in CD8⁺ TILs are mechanisms associated with protective antitumor immunity following PD-1 deletion in MC38 tumors.

To determine the generalizability of our findings, we compared our results with (a) CD8+ TILs from mice with MC38 or CT26 tumors that received therapeutic PD-1 blockade (e.g., anti-PD-1), and (b) CD8+ TILs from patients with diverse types of cancer following checkpoint blockade. In mice, we performed differential gene expression analysis between CD8+ TILs from anti-PD-1-treated versus isotype control-treated mice to generate gene modules that were upregulated or downregulated in anti-PD-1-treated CD8+ TILs from Kumar et al. (2022). In both MC38 and CT26, the upregulated genes following anti-PD-1 treatment showed a significant enrichment in the CD8+ TILs from the inducible PD-1^{del.} mice in our dataset, and the downregulated genes showed a significant enrichment in the CD8+ TILs from the WT control mice in our dataset (Fig. S3 E). Moreover, the differentially expressed genes in our dataset correlated with the differentially expressed genes in both CD8+ TILs from MC38 (Kendall's τ correlation = 0.15, P = 4.8 × 10⁻¹⁰²) and CT26 (Kendall's τ = 0.21, P = 1.7 × 10⁻²⁰⁴) (Table S6).

Next, we compared enrichment of the most elevated topics in CD8⁺ TILs from mice (the top 5 in WT control and the top 5 in the inducible PD-1^{del.}, providing 10 topics in total) with those in CD8⁺ TILs from five cohorts of cancer patients that received checkpoint inhibitors (e.g., anti-PD-1 [pembrolizumab, cemiplimab] and/or anti-PD-1 plus anti-CTLA-4 [ipilimumab plus nivolumab]) (Bassez et al., 2021; Liu et al., 2022; Prakadan et al., 2021; Yost et al., 2019). These cohorts represented diverse cancer types including squamous cell carcinoma, basal cell carcinoma, breast cancer, leptomeningeal disease resulting from metastasis mostly from breast cancer, and non-small-cell lung cancer. These studies were selected because they had pre- and postcheckpoint blockade samples from site-matched tumor tissue. Though there was variability across datasets, there was concordance between our findings from the topics upregulated in CD8+ TILs from inducible PD-1^{del.} mice and some of these human datasets, particularly with enrichment of topics associated with increased IFN

stimulation and effector functions following checkpoint blockade (Fig. 3 F and Table S7). These data suggest that there are conserved transcriptional changes in CD8⁺ TILs following PD-1 genetic deletion and antibody blockade in mice, and between PD-1 genetic deletion and antibody blockade in humans, highlighting the utility of this model to study mechanisms of PD-1-blockade-induced protective antitumor immunity.

Lastly, we evaluated cell cycle and clonal expansion in CD8⁺ TILs between the two genotypes, since increased clonal expansion is often associated with responses to PD-1 blockade both in preclinical models such as LCMV clone 13 and in cancer patients (Barber et al., 2006; Odorizzi et al., 2015; Pauken et al., 2016; Valpione et al., 2020; Wu et al., 2020). To assess a functional readout of the degree of cell division that had occurred, we quantified expansion using the paired scTCR-seq data obtained from each cell along with the scRNA-seq. Because of the high level of TCR diversity in the preimmune T cell repertoire, when the same TCR sequence is observed multiple times in the same host it is generally inferred that clonal expansion has occurred (Pauken et al., 2022). Consequently, the TCR can serve as a molecular barcode to track individual clones through activation, differentiation, and migration across tissues (Pauken et al., 2022). The Simpson indices of CD8+ TIL repertoires from inducible PD-1KO mice were greater than from WT control mice (inducible PD-1^{del.}; Mouse 5 = 0.0709, Mouse 6 = 0.034, WT control; Mouse 3 = 0.028, Mouse 4 = 0.0271, Fig. 3 G), indicating lower diversity in the inducible PD-1^{del.} mice and consequently more clonal expansion; i.e., a small number of T cell clones have preferentially expanded. Collectively, these data support a model where genetic loss of PD-1 results in significant transcriptional changes including IFN stimulation, effector functions, exhaustion, and increased clonal expansion, associated with protective antitumor immunity in MC38 tumors.

Development of a computational method to detect deletion of the *Pdcd1* gene

We next evaluated the relative contribution of CD8⁺ T cell-autonomous versus non-cell-autonomous effects on CD8⁺ TILs following PD-1 loss. To do this, we compared bona fide PD-1^{KO}



CD8+ TILs to PD-1Hi CD8+ TILs with an intact Pdcd1 locus in the same TME. However, one challenge in our model is that the inducible PD-1^{del.} mice lack a reporter to distinguish cells that had deleted PD-1 from cells that expressed low levels of the PD-1 protein but had not deleted PD-1. While most CD8+ TILs in MC38 tumors express high levels of PD-1 (referred to as PD-1 $^{\rm Hi}$, \sim 85%), there is a population of CD8+ TILs in MC38 that is low for the PD-1 protein (referred to as PD-1^{Lo}, ~15%), and this population differs substantially in terms of phenotype and function compared with the PD- 1^{Hi} population (the PD- 1^{Lo} population is more quiescent, while the PD-1^{Hi} population is more activated and/or exhausted, Fig. S4, A-D and Table S8). Thus, though the population of PD-1^{Lo} CD8+ TILs is small in WT MC38 tumors, due to the lack of PD-1 surface expression, this population would be sorted into our group containing true PD-1^{KO} cells. The presence of these contaminating PD-1^{Lo} CD8+ TILs could confound our analyses because it is so different from PD-1^{Hi} TILs in the WT tumor setting (Fig. 4 A, Fig. S4, A-D, and Table S8). To circumvent this issue, we developed a computational method to detect deletion of the relevant exons in the Pdcd1 transcript in the scRNA-seq dataset and used this approach to identify and exclude contaminating PD-1^{Lo} cells from the true PD-1^{KO} population (Fig. 4 A).

To develop a computational tool to classify CD8+ TILs as "PD-1-deleted" or "PD-1-non-deleted," we first examined whether deletion of the relevant exons in the Pdcd1 transcript could be detected in the scRNA-seq dataset (Fig. 4 A). In the PD-1^{f/f} mouse, the Pdcd1 locus contains loxP sites upstream of exon 2 and downstream of exon 4, so when Cre is present, we expect deletion of exons 2-4. We hypothesized that accumulation of reads at the different exons of Pdcd1 could be used to distinguish CD8+ TILs that had truly deleted exons 2-4 of the Pdcd1 gene (PD-1^{KO}) from WT PD-1 $^{\text{Lo}}$ CD8+ TILs within the population of PD-1 $^{\text{Lo}}$ CD8+ TILs in inducible PD-1^{del.} mice. To establish a ground truth of the expected read distribution between PD-1^{Lo} and PD-1^{Hi} CD8+ TILs, we examined read distribution in the WT TME. In PD-1^{Lo} CD8+ TILs in WT control mice, there were very few reads at any of the exons of the Pdcdl locus, consistent with these cells being low for both Pdcdl transcript and PD-1 protein (Fig. 4, B and C). Conversely, in PD-1Hi CD8+ TILs in WT control mice, there were significant numbers of reads detected at exons 1 and 2 (Fig. 4, B and C). Compared with the WT TME, the total PD-1^{Lo} CD8⁺ TIL population in the inducible PD-1^{del.} mice showed few reads at exon 2, but significant read accumulation at exons 1 and 5 (Fig. 4, B and C). Conversely, PD-1Hi CD8+ TILs in inducible PD-1 $^{\rm del.}$ mice and PD-1 $^{\rm Hi}$ in the WT control mice showed similar reads, with significant read accumulation at exons 1 and 2, and less detected at exon 5 than the PD-1^{Lo} cells in the same TME (Fig. 4, B and C). There was minimal detection of exons 3 and 4 in any sample (Fig. 4, B and C). We speculate the reads accumulated at exon 5 in the KO because exons 2-4 were deleted, bringing exon 5 in close proximity to exon 1. This finding demonstrated that deletion of the Pdcdl locus can be detected at the transcript level, highlighting the utility of quantifying read distribution across individual exons as a method to detect gene deletion.

We next sought to classify individual cells as being "predicted Pdcd1 KO" or "predicted Pdcd1 non-KO (or WT)" based on read

distribution across the Pdcdl exons. To do this, we used logistic regression to train a classifier to predict protein PD-1 status based on the read distribution across the five exons of the Pdcd1 locus. The classifier's training features were set to be the distribution of reads across the five exons of Pdcd1 (Fig. 4 D). This model of transcript-based prediction performed extremely well at predicting a cell to be high or low for the PD-1 protein (area under the curve [AUC] = 0.93, Fig. 4 E). In brief, cells predicted to be PD-1 protein-positive had a much larger percentage of reads mapping to exon 2, whereas cells predicted to be PD-1 proteinnegative and therefore deleted for the Pdcd1 locus had a much larger percentage mapping to exon 5 (Fig. 4 D, note linear predictor function). As expected, the PD-1^{Lo} CD8+ TIL compartment in the inducible PD-1^{del.} mice did contain a small population of CD8+ T cells that were predicted to be non-KO PD-1^{Lo} (e.g., PD-1 protein-negative and Pdcd1WT) rather than predicted to be PD-1^{KO} (e.g., PD-1 protein-negative and Pdcd1^{KO}) (Fig. 4, F and G). The predicted non-KO PD-1^{Lo} CD8+ TILs showed elevated expression of genes associated with quiescence (e.g., Tcf7, Sell, Klf2, Malat1, Zfp36l2), whereas predicted PD-1KO CD8+ TILs showed elevated expression of genes associated with exhaustion and/or activation (e.g., Havcr2, Lag3, Lgals1, Irf8) (Fig. 4 H and Table S9). We did observe a small population of cells in the inducible PD- $1^{\mathrm{del.}}$ TME that was predicted to be $\mathit{Pdcd1}^{\mathrm{KO}}$ but also was PD-1 protein-positive (Fig. 4 F, upper right quadrant). These cells may have recently deleted the Pdcd1 locus but have not lost the PD-1 protein yet, or may have been a technical artifact. In order to be as stringent as possible, we selectively compared CD8+ TILs in the inducible PD-1^{del.} mice that were both positive for the PD-1 protein and had predicted to be non-KO for the Pdcd1 locus (Fig. 4 F, lower right quadrant, annotated as PD-1^{Hi}) with CD8+ TILs that were both negative for the PD-1 protein and predicted to be KO based on the absence of reads at exon 2 and the presence of reads at exons 1 and/or 5 (Fig. 4 F, upper left quadrant, annotated to as PD-1^{KO}) (See Materials and methods).

PD-1 deletion on some CD8⁺ TILs can induce a potent antitumor state and improves functions in CD8⁺ TILs still expressing PD-1

Using this novel computational approach to distinguish PD-1^{KO} from non-KO cells, we compared PD-1^{KO} CD8+ TILs and PD-1^{Hi} CD8+ TILs in inducible PD-1^{del.} mice with PD-1^{Hi} and PD-1^{Lo} CD8+ TILs in WT control mice (Fig. 5 A). We sought to determine whether the transcriptional changes observed in the CD8+ TILs following PD-1 deletion were largely due to a cell-intrinsic loss of PD-1, or whether deletion of PD-1 from a proportion of the cells could impact the transcriptional and functional status of CD8+ T cells still expressing PD-1. We first examined the distribution of the transcriptomes of PD-1Hi and PD-1Lo CD8+ TILs in WT control versus PD-1^{Hi} and PD-1^{KO} CD8+ TILs in inducible PD-1^{del.} mice (day 16-17) following deletion of PD-1 from days 7 to 11 using UMAPs (Fig. 5 B and Fig. S1, A-F). In WT control mice, the PD-1Hi and PD-1^{Lo} CD8⁺ TIL populations occupied largely distinct areas of the UMAP (Fig. 5 B), consistent with the phenotypic and functional differences observed between these two populations (Fig. S4, A-D). In contrast, the PD-1^{Hi} and PD-1^{KO} TIL populations from inducible PD-1^{del.} mice showed a remarkably high degree of



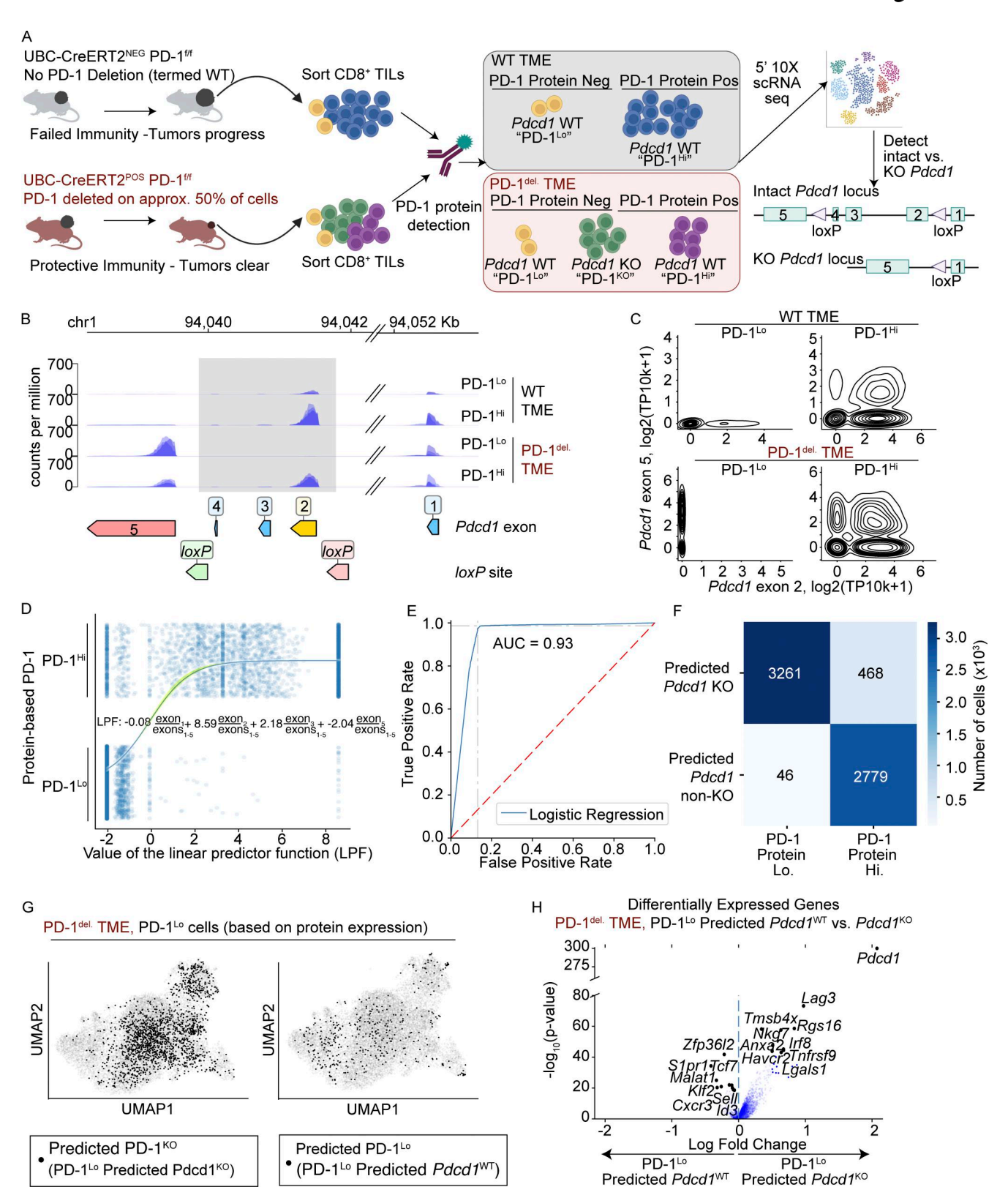


Figure 4. **Development of a computational method to identify T cells that had deleted** *Pdcd1.* **(A)** Schematic for hypothetical cell types (based on PD-1 protein and transcript expression) present in tumors from WT and inducible PD-1^{del.} mice, and the development of a computational method to distinguish true PD-1^{KO} (e.g., cells that have no PD-1 protein and a deletion of the *Pdcd1* gene) from PD-1^{Lo} (e.g., cells that have no PD-1 protein but an intact *Pdcd1* gene) in the single-cell dataset. **(B)** Integrative Genomics Viewer tracks showing the mapping of reads to the individual exons of the *Pdcd1* gene in the scRNA-seq dataset. Samples divided by genotype and PD-1 protein status as indicated in this figure. The locations of the five exons and *loxP* sites are indicated. **(C)** Contour plots showing detection of exon 2 and exon 5 in CD8+ TILs in the scRNA-seq dataset. Plots split up by genotype (WT versus inducible PD-1^{del.}) and PD-1 protein status. **(D)** Logistic regression plot indicating the trained classification model with a solid blue line, with the 95% confidence interval indicated with translucent green



shading. Horizontal axis indicates the linear predictor function of the logistic regression, and vertical axis indicates the PD-1 protein status (based on FACS-based sorting or CITE-seq) with random vertical noise added for visibility of overlapping points. **(E)** ROC curve plot indicating the logistic regression model accuracy for predicting KO status, where PD-1 status (based on FACS-based sorting or CITE-seq) is taken as ground truth. AUC/ROC is indicated (AUC = 0.93). **(F)** Heat map for the confusion matrix showing the number of cells predicted to be KO based on transcript versus non-KO, compared with whether the cell was PD-1 protein–positive or protein–negative (based on FACS-based sorting or CITE-seq). Shown are only cells from the inducible PD-1^{del.} TME. **(G)** UMAP plot showing the distribution of CD8+ TILs from the inducible PD-1^{del.} mice that were low for the PD-1 protein (e.g., PD-1^{Lo} based on FACS-based sorting or CITE-seq) and either predicted to be KO based on the distribution of reads across the five exons (left, shown in black) or predicted to be non-KO (also referred to as WT) (right, shown in black). Gray dots indicate the rest of the cells in the dataset that do not fit that definition. **(H)** Volcano plot showing differential gene expression between PD-1^{Lo} CD8+ TILs from inducible PD-1^{del.} mice (based on protein expression) that were predicted to be $Pdcd1^{KO}$ or $Pdcd1^{KO}$ or $Pdcd1^{KO}$ based on transcript information. Select genes are highlighted. Full list of differentially expressed genes can be found in Table S9. For B–H, shown are cells from two independent experiments representing four mice per genotype. The schematic in A was created with https://BioRender.com.

similarity in terms of distribution on the UMAP (Fig. 5 B). Both PD-1^{Hi} and PD-1^{KO} CD8+ TILs from inducible PD-1^{del.} mice differed substantially from PD-1^{Lo} and PD-1^{Hi} CD8+ TILs from WT control mice, occupying very different transcriptional space than the populations from WT controls (Fig. 5 B). Consistent with the distribution of the four samples across the UMAP, we observed that when applying PCA to the gene expression profiles, the difference in PC1 scores between PD-1^{Lo} and PD-1^{Hi} CD8+ TIL in the WT was large (Cohen's D effect size [CDES]: = -1.446, P = 0), whereas the difference between the PC1 scores for the PD-1 $^{\rm Hi}$ and PD-1 $^{\rm KO}$ in the inducible PD-1 $^{\rm KO}$ TIL was much more modest (CDES = -0.085, P = 0.0037) (Fig. 5 C). These results were consistent across mice and experimental replicates (Fig. S5 A). Additionally, the differences between the PC2-PC10 scores for the PD-1^{Hi} and PD-1^{KO} in the inducible PD-1^{del.} TIL were modest (Fig. S5 B). These differences indicate that many of the transcriptional changes occurring after deletion are similar in PD-1^{KO} and PD-1^{Hi} CD8+ TILs, suggesting that the changes in the antitumor immune response brought about by PD-1 deletion in a proportion of cells are sufficient to affect the differentiation of other CD8+T cells in the TME; i.e., PD-1 deletion can modulate functions in a cell-extrinsic manner.

We next quantified the frequency of cells in each transcriptional cluster in the CD8+ TILs from WT control (PD-1Hi versus PD-1^{Lo}) and inducible PD-1^{del.} (PD-1^{Hi} versus PD-1^{KO}) mice. Consistent with the distribution of the samples within the UMAP (Fig. 5 B), the PD-1^{Lo} and PD-1^{Hi} CD8+ TILs in WT control mice showed a very different distribution across the transcriptional clusters, while the PD-1Hi and PD-1KO CD8+ TILs in inducible PD-1^{del.} mice showed very similar distribution across the transcriptional clusters (Fig. 5 D and Fig. S5, C-E). Relative to the other groups, PD-1^{Lo} CD8⁺ TILs in the WT TME were most overrepresented in Cluster 1 ("quiescent-like/progenitor T cells," Phi coefficient for the PD-1^{Lo} CD8+ TIL group = 0.82882 versus -0.28705, -0.1886, and -0.19909 for the other three groups, P = 0) (Fig. 5 D and Fig. S5, C-E), while the PD-1^{Hi} CD8⁺ TILs in the WT TME were most over-represented in Cluster 2 (immunesuppressed/glycolytic T_{EX} , Phi coefficient for the PD-1 $^{\rm Hi}$ CD8 $^{\rm +}$ TIL group = 0.40041 versus -0.18052, -0.17238, and -0.14847 for the other three groups, P = 0) (Fig. 5 D and Fig. S5, C-E). In contrast, in inducible PD-1^{del.} mice, PD-1^{Hi} and PD-1^{KO} CD8+ TILs both showed over-representation in T_{EX} Cluster 3 ("T_{EX}, terminal," Phi coefficient = 0.30572 and P = 1.039×10^{-247} for PD-1^{KO}, and Phi coefficient = 0.15286 and P = 1.5181 \times 10⁻⁶⁵ for PD-1^{Hi} versus Phi coefficients of -0.1671 and -0.26253 for the other

groups) and Cluster 0 ("IFN-stimulated T_{EX}," Phi coefficient = 0.24896 and P = 3.8104×10^{-168} for PD-1^{KO}, and Phi coefficient = 0.25874 and P = 4.4752×10^{-176} for PD-1^{Hi} [versus Phi coefficients of -0.13757 and -0.3212 for the other groups]) (Fig. 5 D and Fig. S5, C-E). This distribution of cells across the clusters suggested that PD-1^{Hi} CD8+ TILs in inducible PD-1^{del.} mice differed substantially from PD-1Hi CD8+ TILs in WT control mice. Indeed, differential gene expression analysis showed that PD-1Hi CD8+ TILs in inducible PD-1^{del.} mice showed elevated genes associated with IFN stimulation (e.g., Ifit3, Ifit1, Bst2, Isg15, Isg20, Stat1, Usp18), as well as elevated genes associated with cytotoxicity and/or complement activation (e.g., Gzmb, Gzmk) compared with PD-1^{Hi} CD8⁺ TILs in WT control mice (Fig. 5 E and Table S10). Collectively, these data indicate that loss of PD-1 results in transcriptional features associated with increased terminal exhaustion and response to IFN stimulation within CD8+ TILs, and that these changes occur in both PD-1^{KO} and PD-1^{Hi} CD8+ TILs in inducible PD-1^{del.} mice.

To validate these findings, we compared granzyme B protein expression in CD8+ TILs from inducible PD-1^{del.} versus WT control mice by flow cytometry. PD-1 $^{\rm Hi}$ CD8+ TILs in WT control mice had higher expression of granzyme B than PD-1^{Lo} CD8+ TILs (Fig. 5 F), as expected based on previous studies showing that PD-1^{Lo} CD8⁺ T_{EX} are generally more quiescent and/or less activated than PD-1 $^{\rm Hi}$ CD8 $^+$ T $_{\rm EX}$ in both chronic infection and tumors (Fig. S4, A-D) (Blackburn et al., 2008; He et al., 2016; Im et al., 2016; Kurtulus et al., 2019; Miller et al., 2019; Paley et al., 2012). A higher frequency of PD-1^{Lo} CD8+ TILs in inducible PD-1^{KO} mice (which is enriched for PD-1^{KO}) expressed granzyme B compared with PD-1Hi and PD-1Lo CD8+TILs in WT control mice (Fig. 5 F), in accordance with previous work showing that PD-1 loss results in increased levels of granzyme B (Juneja et al., 2017; Kurtulus et al., 2019; Odorizzi et al., 2015). Consistent with our scRNA-seq data, granzyme B protein levels were comparable between the PD- $1^{\rm Hi}$ and PD-1^{Lo} TIL populations in inducible PD-1^{del.} mice (Fig. 5 F), suggesting that PD-1Hi CD8+ TILs show improved functionality in the presence of PD-1^{KO} CD8+ TILs. Collectively, these data support a model where deletion of PD-1 promotes substantial transcriptional reprogramming in the TME and increased cytotoxicity in CD8+ TILs, but a cell-intrinsic deletion of PD-1 is not required for these effects. Rather, PD-1 deletion on some of the CD8⁺ TILs can induce a potent antitumor state that improves the functionality of CD8+ TILs still expressing PD-1, allowing PD-1Hi CD8⁺ TILs to become productive contributors to the antitumor response.



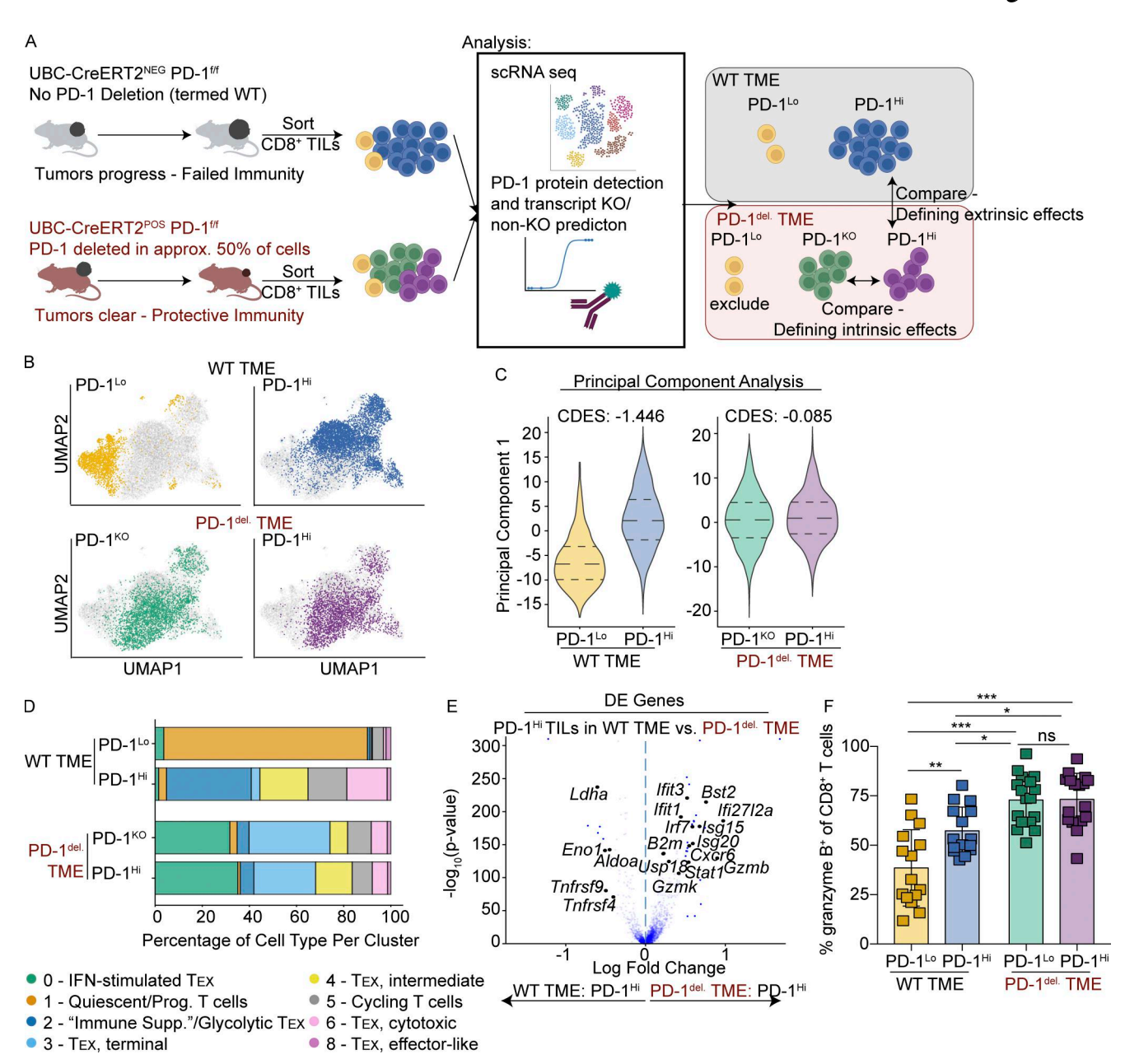


Figure 5. Deletion of PD-1 induces a potent antitumor state and improves functionality in both PD-1^{KO} and PD-1^{HI} CD8+ TILs. (A) Schematic of the experimental design for interrogating the CD8⁺ T cell-intrinsic versus T cell-extrinsic changes following PD-1 deletion. In this figure, a combination of PD-1 protein expression, transcript information, and logistic regression (see Materials and methods) was used to determine whether a CD8⁺ TIL is PD-1^{KO} (based on predicted deletion of the Pdcd1 locus and a lack of PD-1 protein) or PD-1^{Hi} (based on the presence of an intact Pdcd1 locus and the presence of PD-1 protein) in the inducible PD-1^{del}. TME. PD-1^{KO} versus PD-1^{Hi} CD8+ TILs in the inducible PD-1^{del}. TME are compared to define the cell-intrinsic effect of PD-1 deletion, and PD-1^{Hi} CD8+ TILs in the inducible PD-1^{del.} TME are compared with PD-1^{Hi} CD8+ TILs in the WT TME to define the cell-extrinsic effect. The schematic was created with https://BioRender.com. (B) UMAP visualization of CD8+T cells (n = 15,729) sorted from MC38 tumors of WT control versus inducible PD-1^{del.} mice at days 16–17 after tumor implantation. In each UMAP, the color indicates the cells of the given sample (for WT control: PD-1 protein status, and for inducible PD-1^{del.}: both PD-1 protein status and transcript-based prediction for being non-KO or KO) and the cells in the remaining three samples are shown in gray. (c) Violin plots showing the PC1 scores for cells from B. (D) Stacked bar plots showing the frequency of each sample as indicated in the figure belonging to each transcriptional cluster shown in Fig. 3 B. Colors denote transcriptional clusters, labeled with functional annotations (see Materials and methods). A full list of upregulated genes per cluster can be found in Table S1. Clusters are indicated in order from left to right, with Cluster 0 being the left-most cluster, and Cluster 8 being the rightmost cluster. P values generated using Fisher's exact test for all groups across all clusters can be found in Fig. S5 D, and the associated φ coefficients can be found in Fig. S5 E. (E) Differentially expressed (DE) genes between PD-1^{Hi} CD8+ TILs in the WT TME and PD-1^{Hi} CD8+ TILs in the inducible PD-1^{del}. TME. Individual genes of interest are indicated on the plot. The entire list of differentially expressed genes can be found in Table S10. Analyses in B-E include all cells combined from two independent experiments, representing n = 4 mice per genotype. WT TME refers to CD8+ TILs taken from UBC-CreERT2- PD-1^{f/f} mice, and PD-1^{del}. TME refers to CD8+ TILs taken from UBC-CreERT2+ PD-1^{f/f} mice. PD-1^{KO} and PD-1^{Hi} labels on CD8+ TILs were determined as described in Fig. 4 and Materials and methods. (F) Frequency of granzyme B+ PD-1^{Hi} and PD-1^{Lo} CD8+ T cells in MC38 tumors from WT and inducible PD-1^{del}. mice at day 17 after tumor cell implantation assessed using flow cytometry. Data in F are from two experiments combined with n = 15 WT control and n = 17 inducible PD-1^{del}. mice. Data are representative of at least four independent experiments with at least five mice per group. Normality was determined using both the D'Agostino-Pearson



test and Shapiro–Wilk tests, and all groups were considered normally distributed. Significance was assessed using a one-way ANOVA with Tukey's multiple comparisons tests. WT TME PD-1^{Lo} versus WT TME PD-1^{Li}, $P = 0.0044^{**}$; WT TME PD-1^{Lo} versus PD-1^{KO} TME PD-1^{Li}, $P < 0.0001^{***}$; WT TME PD-1^{Li} versus PD-1^{KO} TME PD-1^{Li}, $P < 0.0001^{***}$; WT TME PD-1^{Li} versus PD-1^{KO} TME PD-1^{Li} versus PD-1^{KO} TME PD-1^{Li}, $P < 0.0053^{**}$; PD-1^{KO} TME PD-1^{Li} versus PD-1^{KO} TME PD-1^{Li}, $P < 0.0053^{**}$; PD-1^{KO} TME PD-1^{Li} versus PD-1^{KO} TME PD-1^{Li}, P < 0.0999, ns. All mice received tamoxifen daily from days 7 to 11 i.p. https://BioRender.com.

Cell-intrinsic loss of PD-1 drives increased clonal expansion of PD-1^{KO} CD8⁺ TILs, but PD-1 influences the degree of T cell exhaustion in both a cell-intrinsic and a cell-extrinsic fashion Given that PD-1 $^{\rm Hi}$ CD8 $^+$ TILs exhibited similar function to PD-1 $^{\rm KO}$ TILs in the inducible PD-1^{del.} mice, we next determined how the PD-1^{KO} differed from PD-1^{Hi} TILs to understand cell-intrinsic consequences of PD-1 loss (Fig. 6 A). Differential gene expression analysis showed elevated Gzmk in PD-1KO CD8+ TILs, and Ifitm1, Ifitm2, and other granzymes (e.g., Gzmf, Gzmd, Gzme) in the PD-1^{Hi} CD8+ TILs (Fig. 6 B and Table S11). We also examined the specific impact of PD-1 deletion on clonal expansion, since previous work has shown a critical role of PD-1 in regulating cell cycle (Latchman et al., 2001; Patsoukis et al., 2012; Sharpe and Pauken, 2018), and we had noted an increase in clonal expansion of total CD8+ TILs from inducible PD-1^{del.} versus WT control mice (Fig. 3 G). To evaluate differences between PD-1Hi and PD-1KO CD8+ TILs, we utilized the TCR sequence to group cells into clones based on sharing of the exact TCR sequence on both the alpha chain and the beta chain. Cells were classified as having shared clonotypes if the same TCR sequence was present in both groups within each genotype (i.e., in inducible PD-1^{del.}, PD-1^{KO} versus PD-1 $^{\rm Hi}$ groups, and in WT control, PD-1 $^{\rm Hi}$ versus PD-1 $^{\rm Lo}$ groups). Selecting on the shared clonotypes, we then quantified clonal expansion on a clone-by-clone basis. In the WT control mice, the PD-1^{Lo} group was significantly less expanded than the PD-1^{Hi} group (Fig. 6 C, P = 4.1×10^{-5}). In the inducible PD-1^{del}. mice, the TILs that were predicted to be PD-1^{Lo} (e.g., non-KO and/or no Pdcd1 transcript) were less expanded on a clone-byclone basis than either their PD- $1^{\rm Hi}$ counterparts or their PD- $1^{\rm KO}$ counterparts (data not shown). Conversely, the PD-1^{KO} clones were significantly more expanded than the matching PD-1^{Hi} clones in the inducible PD-1^{del.} mice (Fig. 6 C, P = 8.9×10^{-9}). This finding suggests that despite transcriptional similarities, PD-1 deletion is associated with a greater degree of cell division. Moreover, there was a significant correlation between the fraction of PD-1 $^{\rm KO}$ CD8 $^{\scriptscriptstyle +}$ TILs within a clone and the size of the given clone (Fig. 6 D, KT. corr. = 0.41, $P = 1.52 \times 10^{-7}$), with larger clones containing a larger fraction of PD-1^{KO} cells. Consequently, while the transcriptional changes between PD-1 $^{\rm Hi}$ and PD-1 $^{\rm KO}$ CD8+ TILs were subtle compared with the larger differences between total CD8+ TILs in inducible PD-1^{del.} versus WT control mice, these data suggest that a major cell-intrinsic change following deletion of PD-1 is increased cell division.

We also evaluated how PD-1 deletion affected exhausted T cell subsets in PD-1^{KO} versus PD-1^{Hi} CD8+ TILs. It is well established that there are multiple subsets of CD8+ T_{EX} , with a more "progenitor-like" or quiescent subpopulation expressing high levels of TCF-1 and low levels of IRs including TIM-3, as well as a more "terminally exhausted" population expressing low levels of TCF-1 and high levels of many other IRs including TIM-3 (He et al., 2016; Im et al., 2016; Miller et al., 2019; Sade-Feldman et al.,

2018). As expected, in the WT TME, flow cytometry analyses for TCF-1 and TIM-3 showed that PD-1^{Lo} CD8+ TILs were significantly enriched for the progenitor-like subset, while the PD-1Hi CD8+ TIL population was significantly enriched for the terminally exhausted subset (Fig. 6 E). Previous work has shown that loss of PD-1 signaling resulted in a population-level conversion of the progenitor-like subset to the more terminally exhausted subset (Im et al., 2016; Miller et al., 2019; Odorizzi et al., 2015; Pauken et al., 2016). We therefore hypothesized that a cellintrinsic loss of PD-1 would preferentially drive the conversion of the progenitor pool to more differentiated exhausted subsets. Indeed, flow cytometry studies revealed PD-1^{Lo} CD8+ TILs in inducible PD-1^{del.} mice (which are enriched for PD-1^{KO}) trended toward having a lower frequency of TCF-1+ TIM-3- cells compared with PD-1^{Lo} CD8+ TILs in WT control mice (38.69% in the WT TME and 10.73% in the PD- 1^{KO} TME). Moreover, PD- 1^{Hi} and PD-1^{Lo} CD8+ TILs in the inducible PD-1^{del.} TME showed no significant difference in the frequency of TCF-1+ TIM-3- cells, whereas the PD-1Hi and PD-1Lo CD8+ TILs in the WT TME did show a significant difference in the frequency of TCF-1+ TIM-3cells (Fig. 6 E). Conversely, the PD-1^{Lo} CD8+ TILs in the PD-1^{del.} TME showed a significant increase in the frequency of TIM-3+ TCF-1⁻ cells compared with the PD-1^{Lo} CD8⁺ TILs in the WT TME, and these levels were comparable between the PD-1^{Hi} and PD-1^{Lo} CD8+ TILs in the inducible PD-1^{del.} TME (Fig. 6 E). These data suggest that PD-1 deletion causes a conversion of TCF-1+ progenitor cells to TIM-3+ TCF-1- cells, consistent with previous reports (Im et al., 2016; Miller et al., 2019; Odorizzi et al., 2015; Pauken et al., 2016; Prakadan et al., 2021).

While these data support a model wherein PD-1 deletion precipitates the conversion of the progenitor subset into the terminally exhausted subset, this analysis was limited to a few lineage-defining markers. We used our scRNA-seq data to further examine how PD-1 deletion affected transcriptional signatures associated with multiple different exhausted CD8+ T cell subsets defined in the literature (Beltra et al., 2020; Hudson et al., 2019; Im et al., 2016; Kurtulus et al., 2019; Miller et al., 2019; Pauken et al., 2016), including signatures not only of the progenitor and terminally exhausted subsets, but also of additional subsets that have been identified as intermediate between the progenitor and terminal subsets (Table S2). In WT mice, the PD-1^{Lo} population was enriched for the progenitor-like or naïvelike populations as expected, while the PD-1Hi population was preferentially enriched for signatures associated with cycling populations (Beltra et al., 2020; Miller et al., 2019) (Fig. 6 F). Consistent with expectations based on previous work (Im et al., 2016; Miller et al., 2019; Odorizzi et al., 2015; Pauken et al., 2016), PD-1^{KO} cells displayed enrichment in signatures associated with the more differentiated and/or more exhausted subpopulations, including the terminal T_{EX} population, as well as intermediate $T_{\rm EX}$ or transitory $T_{\rm EX}$ populations (Fig. 6 F). Notably, the PD-1 $^{\rm Hi}$



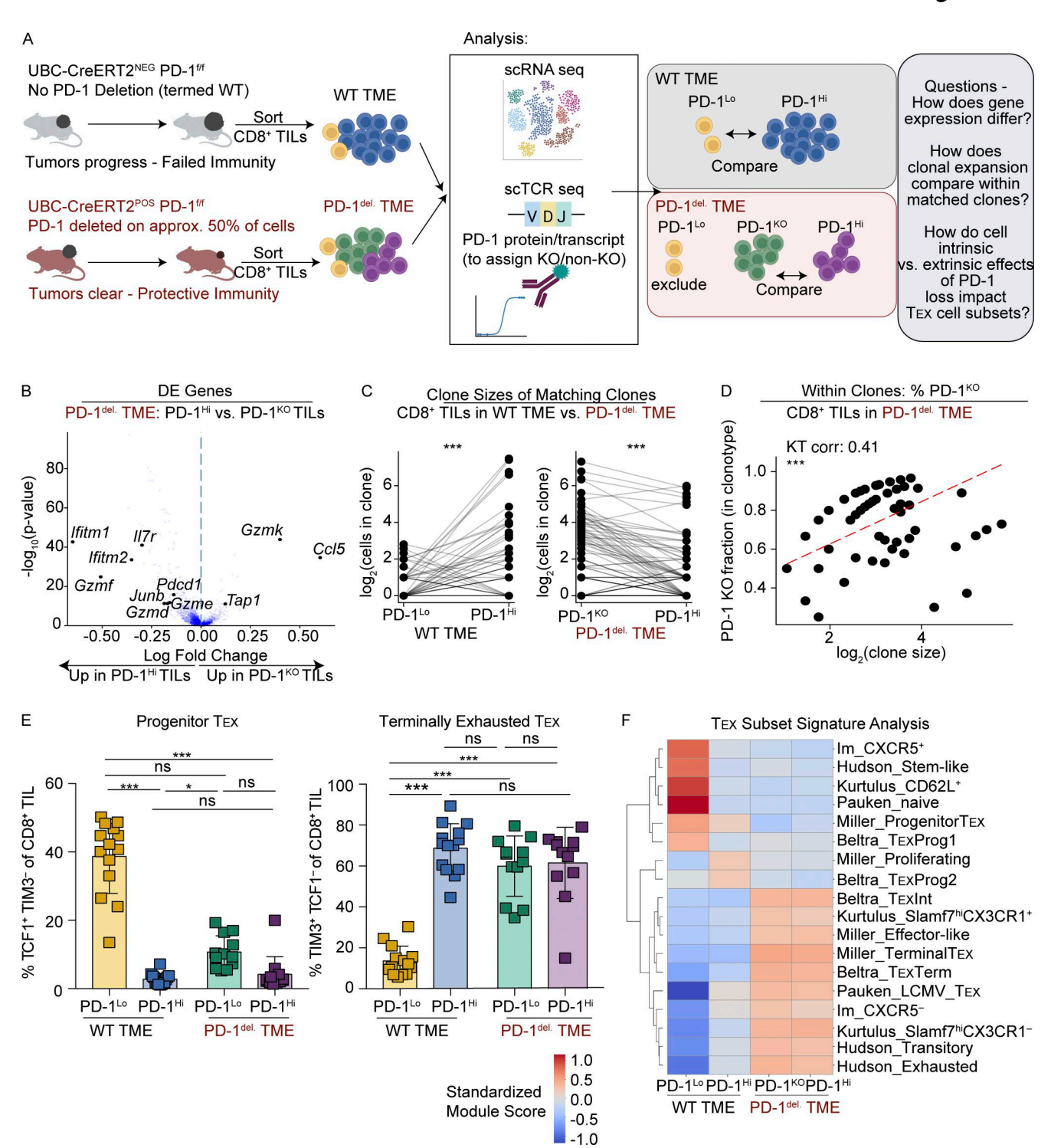


Figure 6. Cell-intrinsic loss of PD-1 drives increased clonal expansion of PD-1^{KO} CD8* TILs compared with PD-1^{Hi} CD8* TILs. (A) Schematic of the experimental design for interrogating the CD8* T cell-intrinsic changes following PD-1 deletion. PD-1^{KO} versus PD-1^{Hi} CD8* TILs in the inducible PD-1^{del.} TME are compared head to head to define the cell-intrinsic effect of PD-1 deletion. The schematic was created with https://BioRender.com. (B) Differentially expressed (DE) genes between PD-1^{Hi} and PD-1^{KO} CD8* TILs in the inducible PD-1^{del.} TME. Individual genes of interest are indicated on the plot. The entire list of differentially expressed genes can be found in Table S11. (C) Quantification of the number of cells within each clonotype, separated by CD8* TILs in the WT TME (left) and inducible PD-1^{del.} TME (right). Cells with a shared TCR sequence are shown as a dot, with lines connecting the dots containing the cells with the same TCR sequence between groups. CDES refers to Cohen's D effect size. Significance was determined used a paired t test. Asterisks (***) indicate P < 0.0001. Exact P values are as follows: WT TME PD-1^{Lo} versus PD-1^{Hi}, P = 4.1 × 10⁻⁵; CDES = -0.93. PD-1^{KO} TME PD-1^{KO} versus PD-1^{Hi}, P = 8.9 × 10⁻⁹; CDES = 0.59. (D) Scatterplot showing the correlation between the fraction of TILs in each clone within the inducible PD-1^{del.} mice that are PD-1^{KO} (y axis) versus the size of the clone (x axis). Asterisks (***) indicate P < 0.0001. Exact P values are as follows: KT correlation = 0.41, P = 1.52 × 10⁻⁷. P value was calculated using the Kendall tau test. (E) Frequency of TCF-1* TIM-3* (progenitor T_{EX}) and TIM-3* TCF-1* (terminal T_{EX}) subpopulations within the PD-1^{Hi} or PD-1^{Lo} CD8* TIL populations in



MC38 tumors from WT versus inducible PD-1^{del}. mice assessed using flow cytometry. Full gating strategy was size, singlets, live, CD45*, CD8 α *, and either PD-1^{l+i} or PD-1^{l-i}. Significance was assessed using the Kruskal–Wallis one-way ANOVA with Dunn's multiple comparisons test. Progenitor T_{EX} (left graph): WT TME PD-1^{l-i} versus WT TME PD-1^{l+i}, $P < 0.0001^{***}$; WT TME PD-1^{l-i} versus PD-1^{del}. TME PD-1^{l-i} versus PD-1^{del}. TME PD-1^{l-i} versus PD-1^{del}. TME PD-1^{l-i} versus PD-1^{del}. TME PD-1^{l-i}, $P < 0.0001^{***}$; WT TME PD-1^{l-i}, P = 0.0886, ns. Terminal T_{EX} (right graph): WT TME PD-1^{l-i} versus WT TME PD-1^{l+i}, $P < 0.0001^{***}$; WT TME PD-1^{l-i} versus PD-1^{del}. TME PD-1^{l-i} versus PD-1^{l-i} versus PD-1^{l-i} versus PD-1^{l-i} versus PD-1^{l-i} in the inducible PD-1^{l-i} versus PD-1^{l-i} versus PD-1^{l-i} versus PD-1^{l-i} in the inducible PD-1^{l-i}

CD8 $^+$ TILs in the inducible PD-1^{del.} mice showed enrichment for the same signatures as PD-1^{KO} (Fig. 6 F), indicating that acquisition of a transcriptional state associated with more differentiated exhausted T cell subsets is not dependent on a CD8 $^+$ T cell-intrinsic loss of PD-1 signaling. Thus, PD-1 can influence the degree of T cell exhaustion in the TME in both a cell-intrinsic and a cell-extrinsic fashion.

Discussion

Decades of evidence support the notion that following PD-1 engagement, cell-intrinsic changes downstream of PD-1 signaling are important for mediating inhibition of T cell functions. However, within the context of the TME, whether the protective effects of PD-1 inhibition are due exclusively to cell-intrinsic changes remains unclear. To elucidate the contributions of the cell-intrinsic and cell-extrinsic effects driving tumor clearance following disrupted PD-1 signaling, we devised an inducible, competitive chimera approach, enabling a head-to-head comparison of PD-1^{Hi} with PD-1^{KO} CD8⁺ T cells in the same TME. Using the precision of comparing the same T cell clones (based on matching TCR sequences) between PD-1^{Hi} and PD-1^{KO} groups, we determined that CD8+ T cells that had lost PD-1 expanded more than CD8+ T cells that had not lost PD-1, consistent with previous reports showing that PD-1 signaling directly inhibits cell cycle (Patsoukis et al., 2020). However, we also observed a notable contribution of cell-extrinsic effects to the phenotype observed following PD-1 deletion. In the inducible PD-1^{del.} TME, PD-1Hi and PD-1KO CD8+ TILs showed similar levels of cytotoxicity and exhaustion. These results demonstrate that the protective effects that occur following PD-1 deletion are not solely restricted to cells with intrinsic loss of PD-1 signaling, and highlight a role of cell-extrinsic remodeling following PD-1 loss promoting antitumor immunity.

Our study suggests loss of PD-1 on some cells can induce a broader change in the TME that feeds back onto PD-1^{Hi} CD8⁺ T cells, allowing those cells to undergo similar transcriptional and functional changes as their PD-1^{KO} counterparts. The precise cellular mechanisms driving the cell-extrinsic improvements in PD-1^{Hi} CD8⁺ T cell functionality are unclear. Previous work has shown that the effector cytokines that CD8⁺ T cells produce, including IFN γ , TNF α , and IL-2, can have profound effects on

antiviral and antitumor immunity, including direct effects on CD8+ T cell functions, other leukocyte populations (e.g., dendritic cells, natural killer cells, B cells), and nonleukocyte populations (e.g., vascular endothelial cells, tumor cells) (Iijima and Iwasaki, 2014; Rosato et al., 2019; Schenkel et al., 2014). We speculate that deletion of PD-1 in some CD8+ TILs results in improved functionality of those cells in a cell-intrinsic manner, including production of inflammatory cytokines, and that these cytokines can feed back on other immune populations in the TME to improve functionality of PD-1Hi CD8+ TILs. Here, CD8+ TILs from the inducible PD-1^{del.} TME showed elevated signs of response to IFN compared with the WT TME, pointing to a role of IFN (either Type I or Type II) in the mechanism of response. This hypothesis is consistent with work showing that elevated IFNy in the TME is associated with better responses to checkpoint blockade in patients (Ayers et al., 2017; Gao et al., 2016; Gocher et al., 2022; Grasso et al., 2020; Shin et al., 2017; Zaretsky et al., 2016). Mechanistically, whether the cell-extrinsic effects of PD-1 deletion are being driven by soluble factors, and whether those soluble factors are acting directly on PD-1Hi CD8+ TIL or whether there are other cell types involved in this process, is not clear. For example, dendritic cell function could be modulated or there could be increased tumor cell killing, causing an increase in antigen presentation to PD-1Hi CD8+ TILs. Future studies parsing out the precise mechanisms contributing to the cell-extrinsic effects following PD-1 loss, including soluble factors such as IFNγ, versus the impact of PD-1^{KO} CD8⁺ T cells on other cell types including dendritic cells and/or Treg cells will be important for identifying potential areas of therapeutic synergy with PD-1 inhibitors.

The CD8+ T cell pool in tumors can be comprised of both tumor antigen-specific T cells that recognize cognate antigen in the tumor, and nontumor antigen-specific or "bystander" T cells that have specificities to other antigens (Meier et al., 2022). Our study demonstrated, through precise TCR matching, that on a clone-by-clone basis, the PD-1^{KO} CD8+ TILs expanded more in the inducible PD-1^{del.} TME than the PD-1^{Hi} cells. However, we did not perform a comprehensive analysis of the behavior of known antigen-specific CD8+ T cell populations in this setting. Future studies are needed to determine whether PD-1 deletion has a preferential effect on tumor antigen-specific populations, and/or influences nontumor antigen-specific or bystander CD8+



T cells in the tumor. Additionally, existing data suggest that PD-1 inhibitors can act in part by promoting the migration of less exhausted CD8+ T cell clones from the periphery into the tumor (Fairfax et al., 2020; Liu et al., 2022; Pauken et al., 2022; Wu et al., 2020; Yost et al., 2019; Zhang et al., 2020). Investigating how partial deletion of PD-1 affects the migration of tumor-specific T cells from the periphery into the tumor, as well as the impact of these recently recruited populations, would be valuable future studies.

Our work using the CD8 conditional PD-1 KO mouse (E8i-Cre) aligns with findings by others (Homet Moreno et al., 2016), demonstrating that PD-1 blockade on CD8+T cells is sufficient for protective immunity in subcutaneous MC38 tumors. A notable advantage of the inducible PD-1^{del.} mouse (UBC-CreERT2) is its ability to ubiquitously delete PD-1 on all PD-1-expressing cell types. Both Treg (CD4+ FoxP3+) and conventional CD4+ (CD4+ FoxP3-) T cells express PD-1 in these tumors (albeit a lower frequency of the populations compared with CD8+ T cells, Fig. 2 D). Interestingly, we found no significant impact on either Treg or conventional CD4⁺ T cell populations in MC38 tumors in the inducible PD-1^{del.} mouse at the time point examined (data not shown). We speculate that the lack of effect on the CD4+ T cell compartment may be due to the dominant role of CD8+ T cells in this model, potentially reflecting the absence of suitable CD4+ T cell neoantigens in WT MC38 tumors. Additional work examining how PD-1 loss affects the phenotype and function of Treg and T follicular helper cells in models where tertiary lymphoid structure development is important for effective antitumor immunity would be of high interest to the field (Schumacher and Thommen, 2022). We also observed a minimal impact on the overall distribution of key macrophage and dendritic cell (DC) populations in this model (data not shown). It should be noted that one limitation in this study is the use of genetic PD-1 KO rather than anti-PD-1 or anti-PD-L1 antibodies. However, our transcriptional analyses revealed that the key changes in the CD8⁺ T cell compartment in total CD8+ TILs isolated from the inducible PD-1^{del.} mouse mirrored those from mice with either MC38 or CT26 treated with anti-PD-1 antibodies (Fig. S3 E and Table S6) (Kumar et al., 2022).

Another limitation of the current study is the use of subcutaneous MC38 colon adenocarcinoma as a primary tumor model. MC38 was chosen due to its exquisite sensitivity to PD-1 inhibitors as a single agent, which enabled us to dissect mechanisms of response effectively. By comparing the changes in CD8+ TILs following PD-1 deletion with publicly available datasets using PD-1 blockade, we demonstrated that the global effects of PD-1 modulation on total CD8+ T cells were consistent between MC38 and CT26 (Kumar et al., 2022) tumor models. Furthermore, we provided evidence that the transcriptional changes observed in CD8+ TILs in MC38 mice were also present in CD8+ TILs from PD-1-responsive human cancers, with the strongest associations found in a dataset from patients with leptomeningeal disease, predominantly metastatic from breast cancer (Prakadan et al., 2021). However, other patient cohorts showed less of a correlation with our data, highlighting how differences in cancer type and/or disease stage can shape transcriptional

changes in CD8⁺ TILs. Consequently, it remains unclear how PD-1 nonresponsive tumors would react to partial loss of PD-1. Additional studies are needed to explore how conserved these mechanisms are across diverse tumor types with varying degrees of responsiveness to PD-1 inhibitors.

In summary, our studies indicate that PD-1 deletion can enhance antitumor immunity through both direct cell-intrinsic effects and indirect cell-extrinsic effects in the TME. The observation that perturbing PD-1 on some cells can elicit broader changes in the TME that result in improved functionality of PD-1^{Hi} CD8+ T cells has important implications for PD-1-based cancer immunotherapy. Identifying the mediators responsible for the increased function of PD-1^{Hi} CD8+ T cells in the inducible PD-1^{del.} TME could reveal targets for potential combination therapies. These findings also have important implications for treatment of adverse events associated with PD-1 blockade, suggesting that PD-1 blockade may induce widespread tissue changes that can affect cells irrespective of their PD-1 expression status.

Materials and methods

Mice

All mice used were on the C57BL/6 genetic background. WT C57BL/6 (JAX stock number 000664), B6.Cq-Tq(UBC-cre/ER-T2)1Ejb/J (UBC^{Cre/ERT2}) (JAX stock number 007001, transgenic mice that express a Cre-ERT2 fusion gene under the control of the human ubiquitin C [UBC] promoter) (Ruzankina et al., 2007), and C57BL/6-Tg(Cd8a-cre)1Itan/J (JAX stock number 008766, which has a Cre-IRES-GFP cassette under the control of the CD8a E8i enhancer to enable deletion in CD8+ T cells but not CD4⁺ T cells) (Maekawa et al., 2008) mice were purchased from The Jackson Laboratory. Germline PD-1^{-/-} mice (Keir et al., 2007) have been previously described. Mice containing a loxPflanked Pdcd1 allele (termed PD-1ff mice) were generated in our laboratory by inserting loxP sites upstream of exon 2 and downstream of exon 4, allowing deletion of exons 2, 3, and 4 that encode the IgV domain, transmembrane domain, and the first cytoplasmic exon of PD-1, and have previously been described (Tan et al., 2021). PD-1^{f/f} mice were bred with the aforementioned Cre strains to generate mouse strains that lack PD-1 constitutively on CD8+ T cells (E8i-CrePOS PD-1f/f) or inducibly lack PD-1 on all cells (UBC-CreERT2^{POS} PD-1^{f/f}). Cre^{POS} PD-1^{f/f} mice refer to mice that are heterozygous for Cre (contain one copy). Cre^{NEG} mice used for all indicated experiments were littermate controls from the breeding that generated CrePOS mice; mice were bred that were heterozygous for Cre (Cre^{POS/NEG} PD-1^{f/f}) or have no copies of Cre ($Cre^{NEG/NEG}$ PD-1^{f/f}) to generate these littermate controls. The mice used for inducible PD-1^{del.} experiments (both UBC-CreERT2POS PD-1f/f and UBC-CreERT2NEG PD-1^{f/f} littermate controls) also contained a Foxp3-GFP reporter (Bettelli et al., 2006) to label regulatory T cells. Tumor cells were implanted into mice between 6 and 10 wk of age. All mice were maintained in specific pathogen-free facilities at Harvard Medical School under standard housing, husbandry, and diet conditions in accordance with Institutional Animal Care and Use Committee (IACUC) and National Institutes of Health (NIH)



guidelines. Animal protocols were approved by the IACUC at Harvard Medical School.

Tumor cell lines and tamoxifen administration

MC38 colon adenocarcinoma cells (a gift from D. Vignali, University of Pittsburgh School of Medicine, Pittsburgh, PA, USA) were cultured in a 37°C incubator with 5% CO2 in DMEM supplemented with 10% FBS and 100 U penicillin and 100 µg streptomycin. Cells were harvested at passages 2-3 after thaw, and mice anesthetized with 2.5% 2,2,2,-tribromoethanol (Avertin) were injected subcutaneously in the flank with 1×10^5 –2.5 × 105 MC38 tumor cells. Starting at 7 days after tumor cell implantation, tumors were measured every 2-3 days (length × width) with calipers, and mice were sacrificed when tumors reached 2 cm³ volume or became ulcerated, or when they developed a body condition of >2 in accordance with IACUC guidelines. Tumor volume was determined using the formula $0.5 \times D \times d^2$, where D is the major axis, and d is the minor axis. Unless otherwise indicated in the figure legends, tumors were harvested from mice between days 16 and 18 after tumor implantation.

Tamoxifen was administered to both WT control mice (e.g., UBC-CreERT2- PD-1^{f/f} mice) and inducible PD-1^{del.} mice (UBC-CreERT2+ PD-1^{f/f} mice) for all experiments utilizing the inducible PD-1^{del.} mice. Tamoxifen binding to ERT2 induces translocation of the CreERT2 complex to the nucleus to delete the *loxP*-flanked region of *Pdcdl*. To prepare tamoxifen solution for injection, tamoxifen (Sigma-Aldrich) was dissolved in ethanol, diluted 1:20 in sunflower oil, and sonicated for 60 min. Doses of 1 mg per mouse of tamoxifen were administered i.p. daily for 5 days. Unless otherwise indicated in the figure legends, tamoxifen was administered from days 7 to 11 after tumor implantation.

Lymphocyte isolation from mouse tissues

Tumors were dissected and mechanically disaggregated. For flow cytometry experiments, a gentleMACS (Miltenyi) was used for disaggregation, whereas for scRNA-seq, scissors were used to mince the tumors. The dissociated tissue was digested with collagenase type I (400 U/ml; Worthington Biochemical) for 20–30 min at 37°C. Samples were then filtered (70 μm) and subjected to a discontinuous Percoll gradient (40%/70%) to enrich lymphocytes.

Spleens were dissected and mechanically disaggregated. Red blood cells were lysed using ACK lysis buffer (Gibco). In vitro stimulations of splenocytes were performed by incubating total splenocytes with 4 $\mu g/ml$ anti-CD3 (clone 145-2C11; BioXCell) and 4 $\mu g/ml$ anti-CD28 (clone 37.51; BioXCell) in a 37°C incubator with 5% CO $_2$ for 24 h prior to analysis of PD-1 expression using flow cytometry.

Flow cytometry and cell sorting

Single-cell suspensions were generated as described above and labeled with LIVE/DEAD Fixable Near-IR Cell Stain (Thermo Fisher Scientific) in PBS. Cells were preincubated with TruStain Fc Receptor Block (anti-mouse CD16/CD32, clone 93; BioLegend), then labeled with extracellular antibodies in PBS supplemented with 2% FBS including: CD3 (clone 145-2C11) and CD8 α (clone 53-

6.7) (from BD); CD45.2 (clone 104), PD-1 (clone RMPI-30), CD44 (IM7), Tim-3 (clone RMT3-23), and CD62L (clone MEL-14) (from BioLegend). For phospho-PD-1 analysis, cells were fixed with intracellular fixation buffer (eBioscience) and then stained with anti-phospho-PD-1 (clone 6G12, BV421) (Bu et al., 2021). For all other intracellular analyses, cells were fixed and permeabilized with the Foxp3/Transcription Factor Staining kit (eBioscience) and then stained with anti-Foxp3 (FJK-16; eBioscience), anti-Ki-67 (B56; BD), anti-granzyme B (GB11; BioLegend), and/or anti-TCF-1 (C63D9; Cell Signaling).

For CITE-seq experiments, labeling with Feature Barcoding antibodies was performed in PBS supplemented with 2% BSA and 0.01% Tween. Each sample was individually labeled with a Hashtag antibody (Mouse 3 was labeled with C0301_TotalSeqC, Mouse 4 was labeled with C0302_TotalSegC, Mouse 5 was labeled with C0303_TotalSeqC, and Mouse 6 was labeled with C0304_TotalSeqC). This was done in case samples needed to be pooled prior to loading onto the 10X Chromium Controller. However, samples did not get pooled, and each sample was run on its own channel. For detection of PD-1 using CITE-seq, cells were labeled with a biotinylated PD-1 antibody (clone RPMI-30), washed, and subsequently labeled with the CITE-seq antibody CO971_TotalSeqC Streptavidin (BioLegend). Samples were acquired on an LSR II (BD Biosciences) or Symphony (BD Biosciences) and analyzed with FlowJo software (TreeStar), or sorted on a FACSAria (BD Biosciences).

Quantification and statistical analysis (of non-sequencingbased data)

Statistical analyses for flow cytometry data were performed with Prism software (GraphPad), and P values of <0.05 were considered statistically significant. Normality was determined prior to performing statistical analyses using the D'Agostino-Pearson omnibus normality tests and the Shapiro-Wilk normality tests. If all groups were normally distributed, then the Gaussian distribution was assumed when selecting statistical tests. If any group was not normally distributed, then the Gaussian distribution was not assumed when selecting statistical tests. We performed t tests on analyses containing only two groups. For unpaired observations, an unpaired t test was used if data were normally distributed, and a Mann-Whitney test was used if data were not normally distributed. For paired observations, a paired t test was used if data were normally distributed, and a Wilcoxon matched-pairs signed rank test was used if the data were not normally distributed. If analyses contained more than two groups, one-way ANOVAs with posttest comparisons were performed. If data were normally distributed, an ordinary oneway ANOVA was performed. If data were not normally distributed, a Kruskal-Wallis test was performed. For multiple comparisons tests, the mean rank of each column was compared with the mean rank of every other column. The specific statistical test used for each plot is indicated in the figure legends. Asterisks indicating significance in each figure are defined in the Figure Legends, and exact P values are given when exact p values could be calculated (e.g., P = 0.0004). If an exact P value could not be calculated, the approximation was give (e.g., P < 0.0001). Statistical tests used for computational analyses are indicated in the



corresponding figure legends and Materials and methods sections.

scRNA-seq of mouse samples

scRNA-seq data for CD8+ T cells from inducible PD-1^{del.} mice (e.g., UBC-CreERT2+ PD-1f/f) versus WT control mice (e.g., UBC- $CreERT2^ PD-1^{f/f}$) were generated from two independent experiments. In both experiments, MC38 tumor cells were implanted into mice subcutaneously in the flank on day 0. All mice (both WT control and inducible PD-1^{del.}) were given daily tamoxifen treatment from days 7 to 11 after tumor cell implantation as described above. CD8+ T cells were sorted from dissociated MC38 tumor tissue at days 16-17 after tumor cell implantation (5-6 days after last tamoxifen dose). In the first experiment, cells were sorted based on both CD8a expression and PD-1 protein expression, and CD8+ PD-1 $^{\rm Hi}$ or CD8+ PD-1 $^{\rm Lo}$ TILs from inducible PD-1^{del.} or WT control mice were run on separate 10X channels, providing roughly equal ratios of PD-1Hi and PD-1^{Lo} cells in each genotype. Two mice of each genotype were pooled for the first experiment (Fig. S1). In the second experiment, total CD8+ TILs were sorted (not based on PD-1 protein levels), and PD-1 protein expression was detected after sequencing using CITE-seq to detect PD-1. CD8+ TILs from individual mice were loaded onto separate 10X channels instead of pooling mice, and two mice for each genotype were run on separate channels (Fig. S1). For both experiments, we performed scRNA-seq and TCR sequencing using the 5' 10X platform (10X Genomics). For the second experiment, we also detected Feature Barcodes to determine PD-1 protein expression using CITE-seq. Gene expression and TCR libraries for mouse samples were generated using the Chromium Single Cell 5' Library and V(D)J Reagent Kit (10X Genomics) according to the manufacturer's recommendations. For samples requiring Feature Barcoding libraries to detect TotalSeqC antibodies (from BioLegend), the Chromium Single Cell 5' Feature Barcode Library Kit (10X Genomics) was used according to the manufacturer's recommendations. Following sorting as described above, ~10,000-12,000 cells per sample were loaded onto each channel of the Chromium Chip, and manufacturer's recommendations were followed with an assumed targeted cell recovery of 2,001-6,000 cells. Libraries were sequenced on a NextSeq sequencer (Illumina) by the Dana-Farber Cancer Institute Sequencing Core. Based on the recommendations provided by 10X Genomics, gene expression libraries and Feature Barcoding libraries were sequenced using 26 × 8 × 91 bp parameters, and TCR libraries were sequenced using the 150 × 8 × 150 bp parameters. A minimum of 20,000 reads per cell for gene expression libraries and 5,000 reads per cell for TCR and Feature Barcoding libraries were sequenced based on the approximate number of cells expected.

Demultiplexing and Read Processing for scRNA-seq data

Raw reads (fastqs) were aligned to the GRCm38/mm10 genome using the Ensembl 84 annotations. These annotations (Mus_musculus.GRCm38.84.gtf) were then filtered (Mus_musculus.GRCm38.84.filtered.gtf) using the cellranger v3.0.2 command:

cellranger mkgtf Mus_musculus.GRCm38.84.gtf Mus_musculus.GRCm38.84.filtered.gtf

- --attribute = gene_biotype:protein_coding
- --attribute = gene_biotype:lincRNA
- --attribute = gene_biotype:antisense
- --attribute = gene_biotype:IG_LV_gene
- --attribute = gene_biotype:IG_V_gene
- --attribute = gene_biotype:IG_V_pseudogene
- --attribute = gene_biotype:IG_D_gene
- --attribute = gene_biotype:IG_J_gene
- --attribute = gene_biotype:IG_J_pseudogene
- --attribute = gene_biotype:IG_C_gene
- --attribute = gene_biotype:IG_C_pseudogene
- --attribute = gene_biotype:TR_V_gene
- --attribute = gene_biotype:TR_V_pseudogene
- --attribute = gene_biotype:TR_D_gene
- --attribute = gene_biotype:TR_J_gene
- --attribute = gene_biotype:TR_J_pseudogene
- --attribute = gene_biotype:TR_C_gene

A cellranger-compatible gene expression reference was then generated from the resultant "gtf" file with the command "cellranger mkref," and a cellranger-compatible vdj reference was similarly created with the command "cellranger mkvdjref." Raw gene expression reads were then generated using the cellranger v3.0.2 command "cellranger count" command, using the following feature reference:

id,name,read,pattern,sequence,feature_type
C0971,C0971_TotalSeqC,R2,5PNNNNNNNNNN(BC)NNNNNN
NNN,5'-ATGCGATCAGACCGA-3',Antibody Capture
Hash1,C0301_TotalSeqB,R2,5PNNNNNNNNNNN(BC)NNNNNN
NNN,5'-ACCCACCAGTAAGAC-3',Antibody Capture
Hash2,C0302_TotalSeqB,R2,5PNNNNNNNNNNN(BC)NNNNNN
NNN,5'-GGTCGAGAGAGCATTCA-3',Antibody Capture
Hash3,C0303_TotalSeqB,R2,5PNNNNNNNNNN(BC)NNNNN
NNN,5'-CTTGCCGCATGTCAT-3',Antibody Capture
Hash4,C0304_TotalSeqB,R2,5PNNNNNNNNNN(BC)NNNNNN
NNN,5'-AAAGCATTCTTCACG-3',Antibody Capture

Gene expression quantification ("counts" matrices) was generated with the command cellranger count with the corresponding reference created as described above. Single-cell V(D)J rearrangements were obtained using the command "cellranger vdj," with the vdj reference described above.

Computational processing of gene expression data from scRNA-seq

All analyses were conducted using Python version 3.7.4 and Scanpy version 1.5.1 with additional utilization of the pandas v1.0.3, anndata v0.7.3, matplotlib v3.2.1, seaborn 0.10.1, numpy v1.18.4, and scipy v1.4.1 packages. All count matrices were combined using anndata's concatenate function. Filtering was first done by removing cells that expressed <500 genes and removing genes that were expressed in <1% of cells. Cells were removed if their gene expression consisted of >5% mitochondrial genes, which were genes that began with "mt-." Finally, cells were removed based on the expression of housekeeping genes,



with cells passing the filtering criteria if they had expression >0 for more than half of the genes in the list. This list is provided in Table S12.

Data were normalized to 10,000 counts per cell using the default Scanpy function "normalize_per_cell" and were subsequently logarithmized using log(1+X), where X is the gene count, and "log" is the natural logarithm. Variable genes were found using the scanpy function "highly_variable_genes" with the min_mean parameter set to 0.0125, max_mean set to 3, and min_disp set to 0.5.

The cells from the CITE-seq experiment (Exp 2) were labeled as either PD-1 $^{\rm Hi}$ or PD-1 $^{\rm Lo}$ based on PD-1 protein expression. The data were twice transformed according to $\log_2(1+X)$, where X is the protein count, and a bimodal distribution was observed. Any cell with PD-1 expression >2.5 was labeled as PD-1 $^{\rm Hi}$. All other cells were labeled as PD-1 $^{\rm Lo}$ (see Fig. S1 D).

GSEA

GSEA was performed as described in Subramanian et al. (2005) using the "preranked" approach, as implemented in the panopticon v0.4 function panopticon.analysis.get_enrichment_score, with arguments "presorted," "use_fgsea," "return_es_curve," and "return_pvalue" set to "True." Gene rankings were determined with the panopticon v0.4 function panopticon.analysis.get_cluster_differential_expression, which computes the common language effect size between groups for each gene. For computing GSEA P values, fgsea v1.30.0 was used, with R v4.4.2.

Co-expression analysis of IRs

For the scRNA-seq data, co-expression of multiple IRs was determined based on positive expression (nonzeros detected for counts) of known co-IR genes. The IRs included were *Havcr2* (encoding Tim-3), *Lag3* (encoding LAG-3), *Tigit* (encoding TIGIT), *Cdl60* (encoding CD160), and *Ctla4* (encoding CTLA-4). We intentionally excluded *Pdcd1* since some cells were from WT control mice, and some cells were from inducible PD-1^{del.} mice, and we did not want to bias the distribution of IRs by including it. For IR co-expression analysis by flow cytometry using protein data, Boolean gating was used in FlowJo (TreeStar) software to determine the number of proteins expressed by each cell. Here, antibodies were used to detect protein levels of Tim-3, LAG-3, CD160, and TIGIT.

Topic modeling

Topic modeling was performed using the Python package lda v3.0.2 with 1,500 iterations. Filtering was done as previously mentioned. All TCR genes (genes that begin with "Tra," "Trb," "Trd," or "Trg") and any genes that were expressed in >98% of all cells were removed prior to topic modeling. The non-normalized count matrix was used to generate topics.

PCA and Leiden clustering

PCA was performed on log(TP10k+1) counts, as implemented in the panopticon v0.3 function panopticon.analysis.generate_incremental_pca. Leiden clusters were generated using the Leiden algorithm (Traag et al., 2019) applied to the 50-principal-

component transformation of the normalized counts, as implemented in the python "leidenalg" package v0.8.9, and called via the panopticon v0.3 function "panopticon.analysis.generate_clustering," with options n_clustering_iterations = 1, first_round_leiden = True, optimized_leiden = False, leiden_nneighbors = 40, leiden_iterations = 100.

Functional annotations of scRNA-seq data

Assignment of functional annotations to Leiden clusters was performed using a combination of upregulated genes per cluster, enrichment of key signatures from the literature, and other metrics that have been used in the literature for defining cell states. First, we broadly sought to label clusters as being "exhausted-like," which are indicated with the "TEX" designation. To do this, we examined two key parameters. The first was the co-expression of multiple IR transcripts, since greater numbers of IRs are associated with more severe exhaustion and more terminally differentiated T_{EX} subsets (Blackburn et al., 2009; He et al., 2016; Im et al., 2016; Paley et al., 2012). For all of the clusters except Cluster 1, the majority of cells expressed 3 or more IR transcripts (Fig. S2, B and C), consistent with the notion that many of the CD8+ TILs in MC38 are exhausted-like. Additionally, we examined enrichment of an exhaustion signature derived from LCMV clone 13 (Pauken et al., 2016), since LCMV clone 13 is commonly used as a gold standard model for exhaustion. Again, all clusters except Cluster 1 and Cluster 5 showed reasonably high enrichment for this exhaustion signature (Fig. S2 D). Lastly, we examined *Tox* expression, since the transcription factor TOX has been associated with exhaustion (Alfei et al., 2019; Khan et al., 2019; Scott et al., 2019; Yao et al., 2019). We observed the highest levels of Tox expression in Clusters 2, 3, 4, and 5 (Fig. S2 A), suggesting that on the spectrum of exhaustion, these clusters would be the most exhausted. Taken together, we gave Clusters 0, 2, 3, 4, 6, 7, and 8 $T_{\rm EX}$ designations.

To characterize the heterogeneity of exhausted T cell populations within our dataset, we took into consideration enrichment of signatures associated with different T_{EX} populations, as well as other signatures associated with key biological functions (e.g., IFN stimulation, cell cycle, glycolysis, oxidative phosphorylation). Additionally, we considered key genes of interest upregulated in different clusters (Table S1) or topics (Table S5), including Sell, Tcf7, Lef1, Ccr7, Il7r, Slpr1, Klf2, Cxcr3, Klrg1, Cx3cr1, Slpr5, Tnf, Ifng, Il2ra, Gzmb, Prf1, Mki67, Slamf6, Pdcd1, Lag3, Tigit, Cdl60, Havcr2, Ctla4, Bst2, Irf1, Irf2, Irf7, Mx1, Ccr6, Rorc, Cxcr6, Itgae, cd69, Tbx21, and Eomes.

Cluster 0, designated IFN-stimulated T_{EX} , showed the elevated expression of key genes associated with IFN stimulation, including Isg15, Ifit1, Bst2, Mx1, Stat1, Usp18 (Table S1 and Fig. S2 A). This cluster also showed the strongest enrichment for the HALLMARK IFN γ response, HALLMARK IFN α response, Gene Ontology "Response to IFN," and HALLMARK inflammatory response signatures (Fig. S2 D and Table S2).

Cluster 1, designated as quiescent-like/progenitor-like T cells (abbreviated "Quiescent/Prog. T cells" in figures), showed elevated expression of key genes associated with either quiescence or the progenitor-like $T_{\rm EX}$ subset including *Tcf7*, *Sell*, *Lef1*, *Klf2*,



and Slamf6 (Table S1 and Fig. S2 A). Cluster 1 also showed an enrichment in signatures from the literature associated with the Progenitor T_{EX} phenotype, including the Progenitor T_{EX} signature from Miller et al. (2019), the stemlike signature (CD101-Tim3-) from Hudson et al. (2019), the T_{EX} -Prog1 signature derived from Beltra et al. (2020), the CD62LPOS Slamf7^{NEG} CX3CR1^{NEG} signature from Kurtulus et al. (2019), a signature derived from CXCR5+ cells from Im et al. (2016), and a naïve signature derived from Pauken et al. (2016) (Fig. S2 D and Table S2).

Cluster 2, designated as immune-suppressed/glycolytic T_{EX} (abbreviated "Immune Supp./Glycolytic T_{EX}" in figures), showed elevated expression of key genes associated with the immune-suppressed phenotype described in Nelson et al. (2019), Schietinger et al. (2012), Watkins et al. (2021), Waugh et al. (2016), as well as genes associated with glycolysis. Genes associated with the immune-suppressed phenotype include Tnfrsfl8, Tnfrsf9, Bhlhe40, Ccr7, Ccr8, Nrp1, and Hifla, and genes associated with glycolysis include Gapdh, Eno1, Aldoa, and Ldha (Table S1 and Fig. S2 A). Cluster 2 also showed enrichment for a signature associated with glycolysis (Fig. S2 D), though not to the same extent as the highly proliferative cluster, Cluster 5 (cycling).

Clusters 3, 4, 6, and 8 are all designated as T_{EX} subsets, with names reflective of uniquely upregulated genes for each cluster. Cluster 3 most closely resembles the "terminal T_{EX} " subset described by others (Beltra et al., 2020; He et al., 2016; Hudson et al., 2019; Im et al., 2016; Miller et al., 2019; Paley et al., 2012), expressing high levels of transcripts including Lag3, Havcr2, Prf1, Gzmb, Tigit, Ccl4, and Cxcr6 (Table S1 and Fig. S2 A) and showing enrichment of the terminally exhausted gene signatures (Fig. S2 D). These signatures included the terminal T_{EX} from Miller et al. (2019), terminal T_{EX} (CD101⁺ Tim-3⁺) subset from Hudson et al. (2019), the "T_{EX}_Term" subset from Beltra et al. (2020), and the CD62L⁻ Slamf7^{hi} CX3CR1⁻ subset from Kurtulus et al. (2019). Cluster 6 was designated "TEX, cytotoxic" because of the expression of transcripts including Prfl, Gzmc, Gzme, Gzmd, Gzmb, Gzmf (Tables S1 and S2; and Fig. S2 A), as well as an enrichment in a "cytotoxicity" gene signature (Fig. S2 D). Cluster 8 was designated as " T_{EX} , effector-like" due to the expression of transcripts including Xcl1, Ccl3, Tnfsf14, Ccl4, Ccl1, Cd160, and Ifnq (Table S1 and Fig. S2 A). Cluster 4 was designated "TEX, intermediate." This cluster expressed transcripts associated with ribosomal proteins (Rps/Rpl genes), Pdcd1, Bhlhe40, Tigit, Nr4a2, and Irf8 (Table S1 and Fig. S2 A). It also appeared exhausted-like due to enrichment of the exhaustion signature from LCMV (Pauken et al., 2016) (Fig. S2 D) and co-expression of multiple IRs, but did not show as strong of an enrichment for the terminally exhausted gene signature as Cluster 3 (Fig. S2 D).

Cluster 5 was designated "cycling" due to the high expression of a number of transcripts associated with cell cycle (e.g., *Tubb5*, *Cdkn3*, *Hmgb1*, *Kif23*, *Top2a*, and *Mki67*) (Table S1) and a strong enrichment for the cell cycle signature from Kowalczyk et al. (2015) (Fig. S2 D and Table S2). This cluster also showed a strong enrichment in the HALLMARK signatures "E2F Targets," "G2M checkpoint," "MTORC1 signaling," and "DNA repair," all consistent with these cells being in active cell cycle (Fig. S2 D).

Lastly, Cluster 7 appeared to contain non-T cells (*Cd14*, *Cd68*, *Csf1r*, *Adgre1*) (Table S1 and Fig. S2 A), which was likely due to a low level of contamination from sorting. This cluster was excluded from all downstream analyses.

Comparison of scRNA-seq data from MC38 with patient datasets

Five human datasets were selected that contained donormatched pre- and post-PD-1 blockade-treated scRNA data. These studies included patients with leptomeningeal disease (multiple different primary histologies, posttreatment samples 21-30 days from initial treatment), triple-negative breast cancer (posttreatment samples 7-11 days from initial treatment), lung cancer (posttreatment samples 42-233 days from initial treatment), basal cell carcinoma (posttreatment samples 21-121 days from initial treatment), and squamous cell carcinoma (posttreatment samples 21-49 days from initial treatment) (Bassez et al., 2021; Liu et al., 2022; Prakadan et al., 2021; Yost et al., 2019). For samples from the lung cancer dataset, where patients contributed multiple posttreatment samples, only the posttreatment sample taken most recently after initial therapy was considered. Topics generated as above were projected onto these human data first by matching mouse to human orthologs, then computing cell-by-cell topic loading with the "transform" method of the LDA object from the lda python package.

Single-cell TCR and clonal analysis

Only cells that had at least one detected alpha chain and one detected beta chain annotated, and no more than two detected alpha or two detected beta chains, were included in the analyses incorporating TCR data. Cells were defined as belonging to the same clone if they had an exact sequence match for both the alpha and the beta chain (or chains, for clones with multiple detected). Clone size was determined by counting the number of cells with a given TCR.

Exon-specific *Pdcd1* counts and the logistic regression model for KO prediction

To quantify the contribution of reads to individual exons of the Pdcd1 transcript, we generated count matrices using the cellranger count command, with a custom gene annotation file (gtf) with the Pdcdl gene replaced by separate "genes" for the five exons, which we labeled Pdcd1-exon 1, Pdcd1-exon 2, Pdcd1-exon 3, Pdcd1-exon 4, and Pdcd1-exon 5. This custom gene annotation was created from the filtered gtf file created as described above, using the panopticon v0.3 command "panopticon createsplit-exon-gtf Mus_musculus.GRCm38.84.filtered.gtf Mus_ musculus.GRCm38.84.filtered.splitPdcd1.gtf Pdcd1." A new, cellranger-compatible reference was then created with this output gtf, as described above, and quantification of counts for each gene was obtained through the cellranger count command, also as above. These raw exon-specific counts were then used to construct a predictive model for protein status (as measured via flow cytometry in Experiment 1, CITE-seq in Experiment 2). This was done by computing a logistic regression model (using the sklearn.linear_model_LogisticRegression class, with random_ state = 0, fit_intercept = False), and regressing the normalized



(by dividing raw Pdcdl exon counts by the per-cell sum over all Pdcd1 exon counts) Pdcd1 exon counts from cells from inducible PD-1^{del.} mice (Mouse 1, Mouse 5, Mouse 6) with at least one Pdcd1 exon count against the cells' protein PD-1 status. Prediction was performed using the sklearn.linear_model.LogisticRegression.predict method, which classifies a cell as being Pdcd1 non-KO or KO on the transcript level based on whether the regression score (predicting the probability of PD-1 protein positivity) is greater than or lesser than 0.5, respectively. Thereafter, cells that were denoted as "PD-1 $^{\rm Hi}$ " or "PD-1 $^{\rm KO}$," except where otherwise specified, are those in which both the predicted transcript expression and actual protein expression were in agreement (e.g., PD-1Hi = PdcdIWT and PD-1 protein-positive, and PD-1^{KO} = Pdcd1^{KO} and PD-1 protein-negative). AUC/ROC (receiver operating characteristic curve) scores between the transcript-based prediction and protein status were computed using the sklearn.metrics.roc_auc_score function.

It should be noted that the logistic regression algorithm was trained on all cells from the inducible PD-1^{del.} mice (Mouse 1, 5, and 6) combined. When using all cells, we got an accuracy of 92%. However, we also tested the strength of the model if we had a testing set versus validation set. For this, we did a random cross-validation (60% training, 40% testing), and still got mean accuracy of 92% (std of 3.8%). If we train on Mouse 1, we get accuracies of 86% and 90% on Mouse 5 and Mouse 6, respectively. If we train only on Mouse 1 and Mouse 6, respectively. If we train only on Mouse 6, we get accuracies of 95% and 86% on Mouse 1 and Mouse 5, respectively. Therefore, we are confident in the ability of the logistic regression to perform on this dataset.

Statistics and visualizations related to TCR repertoires

The Simpson Index was calculated without replacement, as implemented in the panopticon v0.3 function panopticon. analysis.simpson. Pie charts and stacked bar charts indicating the relative contribution of T cell clonotypes to a single sample's TCR repertoire were created with the panopticon v0.3 function panopticon.visualization.repertoire plot, with the option "pie" set to be True or False, respectively.

Statistics and visualization related to gene expression

Differential expression was computed using the log fold change defined as the difference of the arithmetic mean of $\log_2(\text{TP10k+1})$ expression values between groups, and P values were computed via the two-sided Mann–Whitney U test, as implemented in scipy.stats.mannwhitneyu. Volcano plots were generated using the panopticon v0.3 function panopticon.visualization.volcano. Wherever relevant, PCA was computed using the sklearn function sklearn.decomposition.PCA. Wherever relevant, module scores were computed with the panopticon v0.3 function "panopticon.analysis.generate_masked_module_score."

Online supplemental material

There are five supplemental figures supporting the findings in the main figures of this paper. All supplemental figures provide further details on the single-cell dataset of CD8⁺ TILs isolated

from WT versus inducible PD-1^{del.} mice. Fig. S1 details the experimental design for the scRNA-seq experiments and relevant details for each experiment. Included are the frequency of PD-1+ cells in each sample by flow cytometry and/or scRNA-seq, the numbers of cells recovered from each experiment, and the distribution of each sample in the UMAP. Fig. S2 shows the expression of select transcripts, co-expression of IRs, and enrichment of key signatures across the different transcriptional clusters in the single-cell dataset. Fig. S3 shows transcriptional differences between total CD8+ TILs in WT versus inducible PD-1^{del.} mice and comparison with changes in anti-PD-1-treated mice. Also shown is the enrichment of genes from different topics in the UMAP. Fig. S4 provides a comparison of phenotypic, functional, and transcriptional features between PD-1Hi and PD-1^{Lo} CD8+ TILs in MC38 tumors in WT control mice. Fig. S5 shows a quantification of principal components and cluster enrichments between PD-1Hi and PD-1Lo CD8+ TILs in WT mice and PD-1 $^{\rm Hi}$ and PD-1 $^{\rm KO}$ CD8 $^+$ TILs in inducible PD-1 $^{\rm del.}$ mice. There are 12 supplemental tables supporting the findings in the main figures of this paper. Table S1 provides a list of upregulated genes for each cluster in the CD8+ T cell single-cell dataset from MC38 tumors from inducible PD-1^{del.} mice (e.g., UBC-CreERT2⁺ PD-1^{f/f} mice) versus WT control mice (e.g., UBC-CreERT2⁻ PD-1^{f/f} mice). Table S2 provides the gene signatures from or derived from the literature on exhausted CD8+ T cell subsets and/or different biological properties that were used in this study. Table S3 shows differentially expressed genes between CD8+ TILs from inducible PD-1^{del.} mice (e.g., UBC-CreERT2+ PD-1^{f/f} mice) versus WT control mice (e.g., UBC-CreERT2- PD-1f/f mice). Table S4 details pathway analysis between CD8+ TILs from inducible PD-1^{del.} mice (e.g., UBC-CreERT2+ PD-1^{f/f} mice) versus WT control mice (e.g., UBC-CreERT2- PD-1f/f mice). Table S5 shows the top 50 genes by weight for topic modeling (18 topic set) in MC38 tumors from inducible PD-1^{del.} mice (e.g., UBC-CreERT2+ PD-1^{f/f} mice) versus WT control mice (e.g., UBC-CreERT2-PD-1^{f/f} mice), as well as the corresponding weights for the genes in each topic. Table S6 provides a comparison of differentially expressed genes between CD8+ TILs from mice with MC38 or CT26 tumors treated with anti-PD-1 from Kumar et al. (2022) and CD8+ TILs from inducible PD-1^{del.} mice versus control. Table S7 shows the common language effect sizes for the genes in CD8+ TILs from MC38 tumors in inducible PD-1^{del.} versus WT control mice compared with the posttreatment versus pretreatment comparison in select patient datasets. Table S8 shows the differentially expressed genes between PD-1Hi and PD-1Lo CD8+ TILs in WT control mice (e.g., UBC-CreERT2- PD-1f/f mice). Table S9 shows the differentially expressed genes between predicted PD-1^{Lo} but non-KO (e.g., PD-1^{Lo} Pdcd1^{WT}) and predicted PD-1^{KO} (e.g., PD-1^{Lo} Pdcd1^{KO}) CD8+ TILs in inducible PD-1^{del.} mice (e.g., UBC-CreERT2+ PD-1f/f mice). Table S10 shows the differentially expressed genes between PD-1Hi CD8+ TILs in WT control mice (e.g., UBC-CreERT2- PD-1f/f mice) and PD-1Hi CD8+ TILs in inducible PD-1^{del.} mice (e.g., UBC-CreERT2+ PD-1^{f/f} mice). Table S11 shows the differentially expressed genes between PD-1Hi and PD-1^{KO} CD8⁺ TILs in inducible PD-1^{del.} mice (e.g., UBC-CreERT2⁺ PD- $1^{f/f}$ mice). Table S12 is a list of the housekeeping genes used to filter cells in the single-cell dataset.



Data availability

The sequencing data from CD8+ T cells from MC38 tumors in inducible PD-1^{del.} versus WT control mice generated during this study have been deposited to the National Center for Biotechnology Information Gene Expression Omnibus database (Accession number GSE290839; https://www.ncbi.nlm.nih.gov/geo/query/acc.cgi?acc=GSE290839). The panopticon package is available on GitHub at https://github.com/scyrusm/panopticon. Raw and processed scRNA and TCR data are available on the single-cell portal: https://singlecell.broadinstitute.org/single_cell/study/SCP1744/loss-of-pd-1-signals-improves-cd8-tilfunction-in-a-cell-intrinsic-and-cell-extrinsic-manner. The other data and materials that support the findings presented in this study are available from the corresponding author (A.H. Sharpe) upon request.

Acknowledgments

We thank past and present members of the Sharpe laboratory for thoughtful scientific discussions. We thank the Immunology Research Flow Cytometry Core Facility at Harvard Medical School for access to flow cytometry equipment and assistance with flow cytometry-based cell sorting.

This work was supported by NIH P01 AI56299 and P50 CA101942 (to A.H. Sharpe and G.J. Freeman), P01 AI108545 (to A.H. Sharpe), P01 AI39671 (to A.H. Sharpe and M. Singer), and funding from the Evergrande Center for Immunologic Diseases and Gene Lay Institute of Immunology and Inflammation. This work was supported by the Fund for Innovation in Cancer Informatics (to M. Singer). J.M. Schenkel was supported by grants from the NIH (7K08CA256044-3) and is a Cancer Prevention and Research Institute of Texas Scholar in Cancer Research. K.E. Pauken is Andrew Sabin Family Foundation Fellow at The University of Texas MD Anderson Cancer Center. J.M.L. Walsh was supported by the NIH Training Grant 5TL1TR002543. S.C. Markson was supported by the American Association of Immunologists Intersect Fellowship Program for Computational Scientists and Immunologists and the Cancer Research Institute Immuno-Informatics Postdoctoral Fellowship (CRI5009).

Author contributions: K.E. Pauken: conceptualization, data curation, formal analysis, investigation, methodology, validation, visualization, and writing-original draft, review, and editing. S.C. Markson: data curation, formal analysis, methodology, software, visualization, and writing-original draft, review, and editing. T.S. Conway: investigation. V.R. Juneja: conceptualization, investigation, and methodology. O. Shahid: data curation, formal analysis, software, and visualization. K.P. Burke: investigation and writing-review and editing. J.H. Rowe: investigation. T.H. Nguyen: formal analysis, investigation, and writing—review and editing. J.L. Collier: investigation. J.M.L. Walsh: data curation, formal analysis, investigation, and writing-review and editing. M.E. Fung: investigation. J.M. Luber: formal analysis, methodology, and software. A.E. Ringel: investigation. J.M. Schenkel: formal analysis and writingreview and editing. G.J. Freeman: funding acquisition, resources, and writing-review and editing. M.C. Haigis: investigation, methodology, resources, supervision, and writingreview and editing. M. Singer: formal analysis, methodology, software, supervision, and writing—review and editing. A.H. Sharpe: conceptualization, funding acquisition, supervision, and writing—original draft, review, and editing.

Disclosures: V.R. Juneja reported personal fees from BioNTech US, Inc. outside the submitted work. G.J. Freeman reported personal fees from iTeos, Nextpoint, IgM, GV20, Geode, Bio-Entre, Santa Ana Bio, and Simcere of America outside the submitted work; in addition, G.J. Freeman had a patent to the PD-L1/ PD-1 pathway with royalties paid "Roche," a patent to the PD-L1/ PD-1 pathway with royalties paid "Merck MSD," a patent to the PD-L1/PD-1 pathway with royalties paid "AstraZeneca," a patent to the PD-L1/PD-1 pathway with royalties paid "Bristol-Myers Squibb," a patent to the PD-L1/PD-1 pathway with royalties paid "Merck KGA," a patent to the PD-L1/PD-1 pathway with royalties paid "Boehringer Ingelheim," a patent to the PD-L1/ PD-1 pathway licensed "Eli Lilly," a patent to the PD-L1/PD-1 pathway licensed "Coherus Biosciences," and a patent to the PD-L1/PD-1 pathway licensed "Novartis"; and has equity in Nextpoint, iTeos, Invaria, GV20, and Geode. M. Haigis reported grants from ReFuel Bio, personal fees from ReFuel Bio and Mito Q, and "other" from Celine Bio outside the submitted work. M. Singer reported personal fees from Guardant Health outside the submitted work; in addition, M. Singer had a patent to US 2022/ 0347278 A1 pending, a patent to WO 2019/068099 A1 pending, a patent to US 2019/0262399 A1 pending, a patent to WO 2018/ 049025 A3 pending, a patent to WO 2018/049025 A2 pending, a patent to US 2021/0263012 A1 pending, a patent to WO 2019/ 100001 Al pending, a patent to US 2021/0130776 Al pending, a patent to WO 2017/075478 A2 pending, a patent to EP 3368689 B1 pending, a patent to WO 2024/264065 Al pending, a patent to WO 2017/075478 A3 pending, and a patent to WO 2017/075465 Al pending. A.H. Sharpe reported grants from NIH P0156299, NIH P01AI108545, NIH P0139671, NIH P50 CA101942, NIH 7K08CA256044-3, NIH 5TL1TR002543, Fund for Innovation in Cancer Informatics, MD Anderson CPRIT Award, Andrew Sabin Family Foundation, American Association of Immunologists, and Cancer Research Institute during the conduct of the study; personal fees from Surface Oncology, Sq Biotech, Selecta, Elpiscience, Bicara, FibroGen, Alixia, GlaxoSmithKline, Janssen, Amgen, BioEntre, ImmVue, and AltruBio; grants from Merck, Quark Ventures, AbbVie, Moderna, Erasca, Vertex, TaiwanBio, Calico, and Yosemite; and "other" from Monopteros and Corner Therapeutics outside the submitted work; in addition, A.H. Sharpe had a patent number 7,432,059 with royalties paid "Roche, Merck, Bristol-Myers-Squibb, EMD-Serono, Boehringer Ingelheim, AstraZeneca, Leica, Mayo Clinic, Dako and Novartis," a patent number 7,722,868 with royalties paid "Roche, Merck, Bristol-Myers-Squibb, EMD-Serono, Boehringer Ingelheim, AstraZeneca, Leica, Mayo Clinic, Dako and Novartis," a patent number 8,652,465 licensed Roche, a patent number 9,457,080 licensed Roche, a patent number 9,683,048 licensed Novartis, a patent number 9,815,898 licensed Novartis, a patent number 9,845,356 licensed Novartis, a patent number 10,202,454 licensed Novartis, a patent number 10,457,733 licensed Novartis, a patent number 9,580,684 issued none, a patent number



9,988,452 issued none, a patent number 10,370,446 issued none, a patent number 10,457,733 issued none, a patent number 10,752,687 issued none, a patent number 10,851,165 issued none, a patent number 10,934,353 issued none, and a patent number 15,314,251 issued none; and is also on the scientific advisory boards of the Massachusetts General Cancer Center, Program in Cellular and Molecular Medicine at Boston Children's Hospital, the Human Oncology and Pathogenesis Program at Memorial Sloan Kettering Cancer Center, the Johns Hopkins Bloomberg-Kimmel Institute for Cancer Immunotherapy, the Gladstone Institutes, and Perlmutter Cancer Center at New York University and is an academic editor for the Journal of Experimental Medicine. K.E. Pauken reports a patent WO2017165412A3 that is pending. No other disclosures were reported.

Submitted: 30 March 2023 Revised: 17 April 2025 Accepted: 9 June 2025

References

- Alfei, F., K. Kanev, M. Hofmann, M. Wu, H.E. Ghoneim, P. Roelli, D.T. Utzschneider, M. von Hoesslin, J.G. Cullen, Y. Fan, et al. 2019. TOX reinforces the phenotype and longevity of exhausted T cells in chronic viral infection. *Nature*. 571:265–269. https://doi.org/10.1038/s41586-019-1326-9
- Ayers, M., J. Lunceford, M. Nebozhyn, E. Murphy, A. Loboda, D.R. Kaufman, A. Albright, J.D. Cheng, S.P. Kang, V. Shankaran, et al. 2017. IFN-gamma-related mRNA profile predicts clinical response to PD-1 blockade. J. Clin. Invest. 127:2930-2940. https://doi.org/10.1172/JCI91190
- Barber, D.L., E.J. Wherry, D. Masopust, B. Zhu, J.P. Allison, A.H. Sharpe, G.J. Freeman, and R. Ahmed. 2006. Restoring function in exhausted CD8 T cells during chronic viral infection. *Nature*. 439:682–687. https://doi.org/10.1038/nature04444
- Bassez, A., H. Vos, L. Van Dyck, G. Floris, I. Arijs, C. Desmedt, B. Boeckx, M. Vanden Bempt, I. Nevelsteen, K. Lambein, et al. 2021. A single-cell map of intratumoral changes during anti-PD1 treatment of patients with breast cancer. Nat. Med. 27:820–832. https://doi.org/10.1038/s41591-021-01323-8
- Beltra, J.C., S. Manne, M.S. Abdel-Hakeem, M. Kurachi, J.R. Giles, Z. Chen, V. Casella, S.F. Ngiow, O. Khan, Y.J. Huang, et al. 2020. Developmental relationships of four exhausted CD8(+) T cell subsets reveals underlying transcriptional and epigenetic landscape control mechanisms. *Immunity*. 52:825–841.e8. https://doi.org/10.1016/j.immuni.2020.04.014
- Bettelli, E., Y. Carrier, W. Gao, T. Korn, T.B. Strom, M. Oukka, H.L. Weiner, and V.K. Kuchroo. 2006. Reciprocal developmental pathways for the generation of pathogenic effector TH17 and regulatory T cells. *Nature*. 441:235–238. https://doi.org/10.1038/nature04753
- Bhatt, D., B. Kang, D. Sawant, L. Zheng, K. Perez, Z. Huang, L. Sekirov, D. Wolak, J.Y. Huang, X. Liu, et al. 2021. STARTRAC analyses of scRNAseq data from tumor models reveal T cell dynamics and therapeutic targets. J. Exp. Med. 218:e20201329. https://doi.org/10.1084/jem.20201329
- Bielecki, P., S.J. Riesenfeld, J.C. Hütter, E. Torlai Triglia, M.S. Kowalczyk, R.R. Ricardo-Gonzalez, M. Lian, M.C. Amezcua Vesely, L. Kroehling, H. Xu, et al. 2021. Skin-resident innate lymphoid cells converge on a pathogenic effector state. *Nature*. 592:128–132. https://doi.org/10.1038/s41586-021-03188-w
- Blackburn, S.D., H. Shin, G.J. Freeman, and E.J. Wherry. 2008. Selective expansion of a subset of exhausted CD8 T cells by alphaPD-L1 blockade. Proc. Natl. Acad. Sci. USA. 105:15016–15021. https://doi.org/10.1073/pnas
- Blackburn, S.D., H. Shin, W.N. Haining, T. Zou, C.J. Workman, A. Polley, M.R. Betts, G.J. Freeman, D.A.A. Vignali, and E.J. Wherry. 2009. Coregulation of CD8⁺ T cell exhaustion by multiple inhibitory receptors during chronic viral infection. *Nat. Immunol.* 10:29–37. https://doi.org/10.1038/ni.1679
- Bu, X., V.R. Juneja, C.G. Reynolds, K.M. Mahoney, M.T. Bu, K.A. McGuire, S. Maleri, P. Hua, B. Zhu, S.R. Klein, et al. 2021. Monitoring PD-

- 1 phosphorylation to evaluate PD-1 signaling during antitumor immune responses. *Cancer Immunol. Res.* 9:1465–1475. https://doi.org/10.1158/2326-6066.CIR-21-0493
- Dey, K.K., C.J. Hsiao, and M. Stephens. 2017. Visualizing the structure of RNAseq expression data using grade of membership models. *PLoS Genet.* 13: e1006599. https://doi.org/10.1371/journal.pgen.1006599
- Fairfax, B.P., C.A. Taylor, R.A. Watson, I. Nassiri, S. Danielli, H. Fang, E.A. Mahé, R. Cooper, V. Woodcock, Z. Traill, et al. 2020. Peripheral CD8(+) T cell characteristics associated with durable responses to immune checkpoint blockade in patients with metastatic melanoma. Nat. Med. 26:193–199. https://doi.org/10.1038/s41591-019-0734-6
- Gao, J., L.Z. Shi, H. Zhao, J. Chen, L. Xiong, Q. He, T. Chen, J. Roszik, C. Bernatchez, S.E. Woodman, et al. 2016. Loss of IFN-gamma pathway genes in tumor cells as a mechanism of resistance to anti-CTLA-4 therapy. *Cell*. 167:397–404.e9. https://doi.org/10.1016/j.cell.2016.08.069
- Gocher, A.M., C.J. Workman, and D.A.A. Vignali. 2022. Interferon-gamma: Teammate or opponent in the tumour microenvironment? *Nat. Rev. Immunol.* 22:158–172. https://doi.org/10.1038/s41577-021-00566-3
- Grasso, C.S., J. Tsoi, M. Onyshchenko, G. Abril-Rodriguez, P. Ross-Macdonald, M. Wind-Rotolo, A. Champhekar, E. Medina, D.Y. Torrejon, D.S. Shin, et al. 2020. Conserved interferon-gamma signaling drives clinical response to immune checkpoint blockade therapy in melanoma. Cancer Cell. 38:500–515.e3. https://doi.org/10.1016/j.ccell.2020.08.005
- He, R., S. Hou, C. Liu, A. Zhang, Q. Bai, M. Han, Y. Yang, G. Wei, T. Shen, X. Yang, et al. 2016. Follicular CXCR5-expressing CD8⁺ T cells curtail chronic viral infection. *Nature*. 537:412-428. https://doi.org/10.1038/nature19317
- Homet Moreno, B., J.M. Zaretsky, A. Garcia-Diaz, J. Tsoi, G. Parisi, L. Robert, K. Meeth, A. Ndoye, M. Bosenberg, A.T. Weeraratna, et al. 2016. Response to programmed cell death-1 blockade in a murine melanoma syngeneic model requires costimulation, CD4, and CD8 T cells. Cancer Immunol. Res. 4:845–857. https://doi.org/10.1158/2326-6066.CIR-16-0066.
- Hudson, W.H., J. Gensheimer, M. Hashimoto, A. Wieland, R.M. Valanparambil, P. Li, J.X. Lin, B.T. Konieczny, S.J. Im, G.J. Freeman, et al. 2019. Proliferating transitory T cells with an effector-like transcriptional signature emerge from PD-1(+) stem-like CD8(+) T cells during chronic infection. *Immunity*. 51:1043–1058.e4. https://doi.org/10.1016/j.immuni .2019.11.002
- Hui, E., J. Cheung, J. Zhu, X. Su, M.J. Taylor, H.A. Wallweber, D.K. Sasmal, J. Huang, J.M. Kim, I. Mellman, and R.D. Vale. 2017. T cell costimulatory receptor CD28 is a primary target for PD-1-mediated inhibition. *Science*. 355:1428–1433. https://doi.org/10.1126/science.aaf1292
- Iijima, N., and A. Iwasaki. 2014. T cell memory. A local macrophage chemokine network sustains protective tissue-resident memory CD4 T cells. Science. 346:93–98. https://doi.org/10.1126/science.1257530
- Im, S.J., M. Hashimoto, M.Y. Gerner, J. Lee, H.T. Kissick, M.C. Burger, Q. Shan, J.S. Hale, J. Lee, T.H. Nasti, et al. 2016. Defining CD8⁺ T cells that provide the proliferative burst after PD-1 therapy. *Nature*. 537:417-421. https://doi.org/10.1038/nature19330
- Juneja, V.R., K.A. McGuire, R.T. Manguso, M.W. LaFleur, N. Collins, W.N. Haining, G.J. Freeman, and A.H. Sharpe. 2017. PD-L1 on tumor cells is sufficient for immune evasion in immunogenic tumors and inhibits CD8 T cell cytotoxicity. J. Exp. Med. 214:895-904. https://doi.org/10.1084/jem.20160801
- Kalia, V., Y. Yuzefpolskiy, A. Vegaraju, H. Xiao, F. Baumann, S. Jatav, C. Church, M. Prlic, A. Jha, P. Nghiem, et al. 2021. Metabolic regulation by PD-1 signaling promotes long-lived quiescent CD8 T cell memory in mice. Sci. Transl. Med. 13:eaba6006. https://doi.org/10.1126/scitranslmed.aba6006
- Kamphorst, A.O., A. Wieland, T. Nasti, S. Yang, R. Zhang, D.L. Barber, B.T. Konieczny, C.Z. Daugherty, L. Koenig, K. Yu, et al. 2017. Rescue of exhausted CD8 T cells by PD-1-targeted therapies is CD28-dependent. Science. 355:1423-1427. https://doi.org/10.1126/science.aaf0683
- Keir, M.E., G.J. Freeman, and A.H. Sharpe. 2007. PD-1 regulates self-reactive CD8⁺ T cell responses to antigen in lymph nodes and tissues. J. Immunol. 179:5064–5070. https://doi.org/10.4049/jimmunol.179.8.5064
- Khan, O., J.R. Giles, S. McDonald, S. Manne, S.F. Ngiow, K.P. Patel, M.T. Werner, A.C. Huang, K.A. Alexander, J.E. Wu, et al. 2019. TOX transcriptionally and epigenetically programs CD8(+) T cell exhaustion. Nature. 571:211–218. https://doi.org/10.1038/s41586-019-1325-x
- Kowalczyk, M.S., I. Tirosh, D. Heckl, T.N. Rao, A. Dixit, B.J. Haas, R.K. Schneider, A.J. Wagers, B.L. Ebert, and A. Regev. 2015. Single-cell RNA-seq reveals changes in cell cycle and differentiation programs upon aging of hematopoietic stem cells. *Genome Res.* 25:1860–1872. https://doi.org/10.1101/gr.192237.115



- Kumar, N., S. Papillon-Cavanagh, H. Tang, S. Wang, C. Stromko, C.P. Ho, S. Soni-Sheth, S. Vasquez-Grinnell, M.L. Broz, D.J. Tenney, et al. 2022. A multi-omic single cell sequencing approach to develop a CD8 T cell specific gene signature for anti-PD1 response in solid tumors. *Int. J. Cancer.* 151:2043–2054. https://doi.org/10.1002/ijc.34218
- Kurtulus, S., A. Madi, G. Escobar, M. Klapholz, J. Nyman, E. Christian, M. Pawlak, D. Dionne, J. Xia, O. Rozenblatt-Rosen, et al. 2019. Checkpoint blockade immunotherapy induces dynamic changes in PD-1(-)CD8(+) tumor-infiltrating T cells. *Immunity*. 50:181-194.e6. https://doi.org/10.1016/j.immuni.2018.11.014
- Latchman, Y., C.R. Wood, T. Chernova, D. Chaudhary, M. Borde, I. Chernova, Y. Iwai, A.J. Long, J.A. Brown, R. Nunes, et al. 2001. PD-L2 is a second ligand for PD-1 and inhibits T cell activation. *Nat. Immunol.* 2:261–268. https://doi.org/10.1038/85330
- Liu, B., X. Hu, K. Feng, R. Gao, Z. Xue, S. Zhang, Y. Zhang, E. Corse, Y. Hu, W. Han, and Z. Zhang. 2022. Temporal single-cell tracing reveals clonal revival and expansion of precursor exhausted T cells during anti-PD-1 therapy in lung cancer. *Nat. Cancer*. 3:108–121. https://doi.org/10.1038/s43018-021-00292-8
- Maekawa, Y., Y. Minato, C. Ishifune, T. Kurihara, A. Kitamura, H. Kojima, H. Yagita, M. Sakata-Yanagimoto, T. Saito, I. Taniuchi, et al. 2008. Notch2 integrates signaling by the transcription factors RBP-J and CREB1 to promote T cell cytotoxicity. Nat. Immunol. 9:1140-1147. https://doi.org/10.1038/ni.1649
- Meier, S.L., A.T. Satpathy, and D.K. Wells. 2022. Bystander T cells in cancer immunology and therapy. *Nat. Cancer.* 3:143–155. https://doi.org/10.1038/s43018-022-00335-8
- Miller, B.C., D.R. Sen, R. Al Abosy, K. Bi, Y.V. Virkud, M.W. LaFleur, K.B. Yates, A. Lako, K. Felt, G.S. Naik, et al. 2019. Subsets of exhausted CD8(+) T cells differentially mediate tumor control and respond to checkpoint blockade. Nat. Immunol. 20:326–336. https://doi.org/10.1038/s41590-019-0312-6
- Nelson, C.E., E.A. Thompson, C.F. Quarnstrom, K.A. Fraser, D.M. Seelig, S. Bhela, B.J. Burbach, D. Masopust, and V. Vezys. 2019. Robust iterative stimulation with self-antigens overcomes CD8(+) T cell tolerance to self-and tumor antigens. Cell Rep. 28:3092–3104.e5. https://doi.org/10.1016/j.celrep.2019.08.038
- Odorizzi, P.M., K.E. Pauken, M.A. Paley, A. Sharpe, and E.J. Wherry. 2015. Genetic absence of PD-1 promotes accumulation of terminally differentiated exhausted CD8+ T cells. J. Exp. Med. 212:1125–1137. https://doi.org/10.1084/jem.20142237
- Paley, M.A., D.C. Kroy, P.M. Odorizzi, J.B. Johnnidis, D.V. Dolfi, B.E. Barnett, E.K. Bikoff, E.J. Robertson, G.M. Lauer, S.L. Reiner, and E.J. Wherry. 2012. Progenitor and terminal subsets of CD8⁺ T cells cooperate to contain chronic viral infection. *Science*. 338:1220–1225. https://doi.org/ 10.1126/science.1229620
- Parry, R.V., J.M. Chemnitz, K.A. Frauwirth, A.R. Lanfranco, I. Braunstein, S.V. Kobayashi, P.S. Linsley, C.B. Thompson, and J.L. Riley. 2005. CTLA-4 and PD-1 receptors inhibit T-cell activation by distinct mechanisms. Mol. Cell. Biol. 25:9543–9553. https://doi.org/10.1128/MCB.25.21.9543-9553-2005
- Patsoukis, N., D. Sari, and V.A. Boussiotis. 2012. PD-1 inhibits T cell proliferation by upregulating p27 and p15 and suppressing Cdc25A. Cell Cycle. 11:4305–4309. https://doi.org/10.4161/cc.22135
- Patsoukis, N., Q. Wang, L. Strauss, and V.A. Boussiotis. 2020. Revisiting the PD-1 pathway. Sci. Adv. 6:eabd2712. https://doi.org/10.1126/sciadv.abd2712
- Pauken, K.E., J. Godec, P.M. Odorizzi, K.E. Brown, K.B. Yates, S.F. Ngiow, K.P. Burke, S. Maleri, S.M. Grande, L.M. Francisco, et al. 2020. The PD-1 pathway regulates development and function of memory CD8(+) T cells following respiratory viral infection. Cell Rep. 31:107827. https://doi.org/10.1016/j.celrep.2020.107827
- Pauken, K.E., K.A. Lagattuta, B.Y. Lu, L.E. Lucca, A.I. Daud, D.A. Hafler, H.M. Kluger, S. Raychaudhuri, and A.H. Sharpe. 2022. TCR-Sequencing in cancer and autoimmunity: Barcodes and beyond. *Trends Immunol.* 43: 180–194. https://doi.org/10.1016/j.it.2022.01.002
- Pauken, K.E., M.A. Sammons, P.M. Odorizzi, S. Manne, J. Godec, O. Khan, A.M. Drake, Z. Chen, D.R. Sen, M. Kurachi, et al. 2016. Epigenetic stability of exhausted T cells limits durability of reinvigoration by PD-1 blockade. Science. 354:1160–1165. https://doi.org/10.1126/science aaf2807
- Pauken, K.E., O. Shahid, K.A. Lagattuta, K.M. Mahuron, J.M. Luber, M.M. Lowe, L. Huang, C. Delaney, J.M. Long, M.E. Fung, et al. 2021a. Single-cell analyses identify circulating anti-tumor CD8 T cells and markers for their enrichment. J. Exp. Med. 218:e20200920. https://doi.org/10.1084/jem.20200920

- Pauken, K.E., J.A. Torchia, A. Chaudhri, A.H. Sharpe, and G.J. Freeman. 2021b. Emerging concepts in PD-1 checkpoint biology. Semin. Immunol. 52: 101480. https://doi.org/10.1016/j.smim.2021.101480
- Pauken, K.E., and E.J. Wherry. 2015. Overcoming T cell exhaustion in infection and cancer. Trends Immunol. 36:265–276. https://doi.org/10.1016/j.it.2015.02.008
- Prakadan, S.M., C.A. Alvarez-Breckenridge, S.C. Markson, A.E. Kim, R.H. Klein, N. Nayyar, A.W. Navia, B.M. Kuter, K.E. Kolb, I. Bihun, et al. 2021. Genomic and transcriptomic correlates of immunotherapy response within the tumor microenvironment of leptomeningeal metastases. Nat. Commun. 12:5955. https://doi.org/10.1038/s41467-021-25860-5
- Pritchard, J.K., M. Stephens, and P. Donnelly. 2000. Inference of population structure using multilocus genotype data. Genetics. 155:945–959. https://doi.org/10.1093/genetics/155.2.945
- Raghavan, S., N. Tovbis-Shifrin, C. Kochel, A. Sawant, M. Mello, M. Sathe, W. Blumenschein, E.S. Muise, A. Chackerian, E.M. Pinheiro, et al. 2021. Conditional deletion of Pdcd1 identifies the cell-intrinsic action of PD-1 on functional CD8 T cell subsets for antitumor efficacy. Front. Immunol. 12:752348. https://doi.org/10.3389/fimmu.2021.752348
- Ribas, A., and J.D. Wolchok. 2018. Cancer immunotherapy using checkpoint blockade. Science. 359:1350-1355. https://doi.org/10.1126/science.aar4060
- Rosato, P.C., S. Wijeyesinghe, J.M. Stolley, C.E. Nelson, R.L. Davis, L.S. Manlove, C.A. Pennell, B.R. Blazar, C.C. Chen, M.A. Geller, et al. 2019. Virus-specific memory T cells populate tumors and can be repurposed for tumor immunotherapy. *Nat. Commun.* 10:567. https://doi.org/10.1038/s41467-019-08534-1
- Ruzankina, Y., C. Pinzon-Guzman, A. Asare, T. Ong, L. Pontano, G. Cotsarelis, V.P. Zediak, M. Velez, A. Bhandoola, and E.J. Brown. 2007. Deletion of the developmentally essential gene ATR in adult mice leads to agerelated phenotypes and stem cell loss. Cell Stem Cell. 1:113–126. https:// doi.org/10.1016/j.stem.2007.03.002
- Sade-Feldman, M., K. Yizhak, S.L. Bjorgaard, J.P. Ray, C.G. de Boer, R.W. Jenkins, D.J. Lieb, J.H. Chen, D.T. Frederick, M. Barzily-Rokni, et al. 2018. Defining T cell states associated with response to checkpoint immunotherapy in melanoma. Cell. 175:998-1013.e20. https://doi.org/10.1016/j.cell.2018.10.038
- Schenkel, J.M., K.A. Fraser, L.K. Beura, K.E. Pauken, V. Vezys, and D. Masopust. 2014. T cell memory. Resident memory CD8 T cells trigger protective innate and adaptive immune responses. Science. 346:98–101. https://doi.org/10.1126/science.1254536
- Schietinger, A., J.J. Delrow, R.S. Basom, J.N. Blattman, and P.D. Greenberg. 2012. Rescued tolerant CD8 T cells are preprogrammed to reestablish the tolerant state. *Science*. 335:723-727. https://doi.org/10.1126/science. 1214277
- Schumacher, T.N., and D.S. Thommen. 2022. Tertiary lymphoid structures in cancer. Science. 375:eabf9419. https://doi.org/10.1126/science.abf9419
- Scott, A.C., F. Dündar, P. Zumbo, S.S. Chandran, C.A. Klebanoff, M. Shakiba, P. Trivedi, L. Menocal, H. Appleby, S. Camara, et al. 2019. TOX is a critical regulator of tumour-specific T cell differentiation. *Nature*. 571: 270–274. https://doi.org/10.1038/s41586-019-1324-y
- Sharma, P., and J.P. Allison. 2015a. The future of immune checkpoint therapy. Science. 348:56–61. https://doi.org/10.1126/science.aaa8172
- Sharma, P., and J.P. Allison. 2015b. Immune checkpoint targeting in cancer therapy: Toward combination strategies with curative potential. *Cell*. 161:205-214. https://doi.org/10.1016/j.cell.2015.03.030
- Sharpe, A.H., and K.E. Pauken. 2018. The diverse functions of the PD1 inhibitory pathway. Nat. Rev. Immunol. 18:153-167. https://doi.org/10 .1038/nri.2017.108
- Shin, D.S., J.M. Zaretsky, H. Escuin-Ordinas, A. Garcia-Diaz, S. Hu-Lieskovan, A. Kalbasi, C.S. Grasso, W. Hugo, S. Sandoval, D.Y. Torrejon, et al. 2017. Primary resistance to PD-1 blockade mediated by JAK1/2 mutations. Cancer Discov. 7:188–201. https://doi.org/10.1158/2159-8290.CD-16-1223
- Subramanian, A., P. Tamayo, V.K. Mootha, S. Mukherjee, B.L. Ebert, M.A. Gillette, A. Paulovich, S.L. Pomeroy, T.R. Golub, E.S. Lander, et al. 2005. Gene set enrichment analysis: A knowledge-based approach for interpreting genome-wide expression profiles. *Proc. Natl. Acad. Sci. USA*. 102: 15545–15550. https://doi.org/10.1073/pnas.0506580102
- Tan, C.L., J.R. Kuchroo, P.T. Sage, D. Liang, L.M. Francisco, J. Buck, Y.R. Thaker, Q. Zhang, S.L. McArdel, V.R. Juneja, et al. 2021. PD-1 restraint of regulatory T cell suppressive activity is critical for immune tolerance. J. Exp. Med. 218:e20182232. https://doi.org/10.1084/jem.20182232
- Topalian, S.L., J.M. Taube, R.A. Anders, and D.M. Pardoll. 2016. Mechanism-driven biomarkers to guide immune checkpoint blockade in cancer therapy. Nat. Rev. Cancer. 16:275–287. https://doi.org/10.1038/nrc.2016.36



- Topalian, S.L., J.M. Taube, and D.M. Pardoll. 2020. Neoadjuvant checkpoint blockade for cancer immunotherapy. *Science*. 367:eaax0182. https://doi.org/10.1126/science.aax0182
- Traag, V.A., L. Waltman, and N.J. Van Eck. 2019. From louvain to leiden: Guaranteeing well-connected communities. Sci. Rep. 9:5233. https://doi.org/10.1038/s41598-019-41695-z
- Valpione, S., E. Galvani, J. Tweedy, P.A. Mundra, A. Banyard, P. Middlehurst, J. Barry, S. Mills, Z. Salih, J. Weightman, et al. 2020. Immuneawakening revealed by peripheral T cell dynamics after one cycle of immunotherapy. Nat. Cancer. 1:210–221. https://doi.org/10.1038/s43018 -019-0022-x
- Vesely, M.D., T. Zhang, and L. Chen. 2022. Resistance mechanisms to anti-PD cancer immunotherapy. Annu. Rev. Immunol. 40:45-74. https://doi.org/10.1146/annurev-immunol-070621-030155
- Watkins, E.A., J.T. Antane, J.L. Roberts, K.M. Lorentz, S. Zuerndorfer, A.C. Dunaif, L.J. Bailey, A.C. Tremain, M. Nguyen, R.C. De Loera, et al. 2021. Persistent antigen exposure via the eryptotic pathway drives terminal T cell dysfunction. Sci. Immunol. 6:eabe1801. https://doi.org/10.1126/sciimmunol.abe1801
- Waugh, K.A., S.M. Leach, B.L. Moore, T.C. Bruno, J.D. Buhrman, and J.E. Slansky. 2016. Molecular profile of tumor-specific CD8⁺ T cell hypofunction in a transplantable murine cancer model. J. Immunol. 197: 1477–1488. https://doi.org/10.4049/jimmunol.1600589
- Wei, S.C., J.H. Levine, A.P. Cogdill, Y. Zhao, N.-A.A.S. Anang, M.C. Andrews, P. Sharma, J. Wang, J.A. Wargo, D. Pe'er, and J.P. Allison. 2017. Distinct cellular mechanisms underlie anti-CTLA-4 and anti-PD-1 checkpoint blockade. Cell. 170:1120–1133.e17. https://doi.org/10.1016/j.cell.2017.07 .024
- Woo, S.R., M.E. Turnis, M.V. Goldberg, J. Bankoti, M. Selby, C.J. Nirschl, M.L. Bettini, D.M. Gravano, P. Vogel, C.L. Liu, et al. 2012. Immune inhibitory molecules LAG-3 and PD-1 synergistically regulate T-cell function to promote tumoral immune escape. Cancer Res. 72:917–927. https://doi.org/10.1158/0008-5472.CAN-11-1620

- Wu, T.D., S. Madireddi, P.E. de Almeida, R. Banchereau, Y.-J.J. Chen, A.S. Chitre, E.Y. Chiang, H. Iftikhar, W.E. O'Gorman, A. Au-Yeung, et al. 2020. Peripheral T cell expansion predicts tumour infiltration and clinical response. *Nature*. 579:274–278. https://doi.org/10.1038/s41586-020-2056-8
- Yao, C., H.W. Sun, N.E. Lacey, Y. Ji, E.A. Moseman, H.Y. Shih, E.F. Heuston, M. Kirby, S. Anderson, J. Cheng, et al. 2019. Single-cell RNA-seq reveals TOX as a key regulator of CD8(+) T cell persistence in chronic infection. Nat. Immunol. 20:890–901. https://doi.org/10.1038/s41590-019-0403-4
- Yokosuka, T., M. Takamatsu, W. Kobayashi-Imanishi, A. Hashimoto-Tane, M. Azuma, and T. Saito. 2012. Programmed cell death 1 forms negative costimulatory microclusters that directly inhibit T cell receptor signaling by recruiting phosphatase SHP2. J. Exp. Med. 209:1201–1217. https://doi.org/10.1084/jem.20112741
- Yost, K.E., A.T. Satpathy, D.K. Wells, Y. Qi, C. Wang, R. Kageyama, K.L. McNamara, J.M. Granja, K.Y. Sarin, R.A. Brown, et al. 2019. Clonal replacement of tumor-specific T cells following PD-1 blockade. Nat. Med. 25:1251-1259. https://doi.org/10.1038/s41591-019-0522-3
- Zaretsky, J.M., A. Garcia-Diaz, D.S. Shin, H. Escuin-Ordinas, W. Hugo, S. Hu-Lieskovan, D.Y. Torrejon, G. Abril-Rodriguez, S. Sandoval, L. Barthly, et al. 2016. Mutations associated with acquired resistance to PD-1 blockade in melanoma. N. Engl. J. Med. 375:819–829. https://doi.org/10.1056/NEJMoa1604958
- Zhang, J., Z. Ji, J.X. Caushi, M. El Asmar, V. Anagnostou, T.R. Cottrell, H.Y. Chan, P. Suri, H. Guo, T. Merghoub, et al. 2020. Compartmental analysis of T-cell clonal dynamics as a function of pathologic response to neo-adjuvant PD-1 blockade in resectable non-small cell lung cancer. Clin. Cancer Res. 26:1327-1337. https://doi.org/10.1158/1078-0432.CCR-19-2931
- Zinselmeyer, B.H., S. Heydari, C. Sacristán, D. Nayak, M. Cammer, J. Herz, X. Cheng, S.J. Davis, M.L. Dustin, and D.B. McGavern. 2013. PD-1 promotes immune exhaustion by inducing antiviral T cell motility paralysis. J. Exp. Med. 210:757-774. https://doi.org/10.1084/jem.20121416



Supplemental material



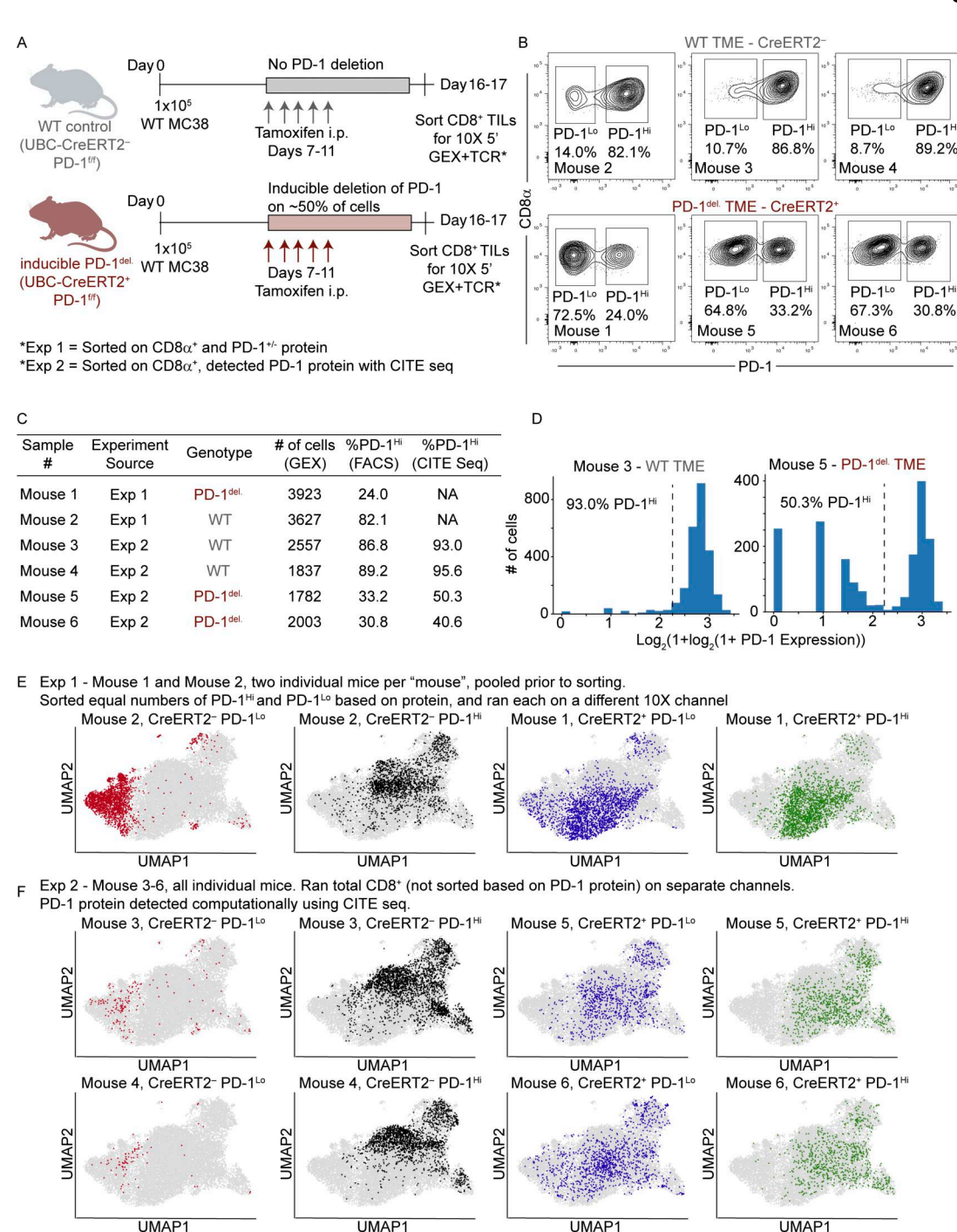


Figure S1. **Generation of scRNA-seq and paired TCR-seq data on CD8*** **TILs from MC38 tumors in inducible PD-1**^{del.} **mice. (A)** Schematic of the experimental design for the scRNA-seq experiments. For Experiment (Exp) 1, roughly equal numbers of PD-1^{Hi} and PD-1^{Lo} CD8* TILs were sorted from UBC-CreERT2* PD-1^{f/f} mice (referred to as inducible PD-1^{del.} mice) or UBC-CreERT2* PD-1^{f/f} mice (referred to as WT control mice) on day 17 (following administration of tamoxifen from days 7 to 11) and loaded onto the 10X Chromium Controller. Two mice were pooled for each genotype. For Experiment 2, total CD8* TILs were sorted from UBC-CreERT2* PD-1^{f/f} mice or UBC-CreERT2* PD-1^{f/f} mice on day 16 (following administration of tamoxifen from days 7 to 11) and loaded onto the 10X Chromium Controller, and PD-1 protein status was determined computationally by detection of PD-1 using CITE-seq. One mouse per genotype was run per channel, and two channels (so two mice) were run per genotype. Schematic was created with https://BioRender.com. **(B)** Flow cytometry contour plots showing the frequency of PD-1^{Hi} and PD-1^{Lo} CD8* TILs in each of the samples that were loaded on the 10X Chromium Controller. An aliquot of each sample was subjected to fluorescent-based PD-1 protein analysis using flow cytometry to confirm expected frequencies of PD-1^{Hi} and PD-1^{Lo}. **(C)** Sample details from 10X runs. **(D)** Representative histograms of distribution of counts for PD-1 CITE-seq (Feature Barcode detection). Shown is one mouse of each genotype from Experiment 2 (Mouse 3 = WT control, Mouse 5 = inducible PD-1^{del.}), representative of both mice in each genotype in this experiment. A threshold was PD-1^{Lo}. **(E)** Distribution of each sample based on genotype (WT versus inducible PD-1^{del.}) and PD-1 protein status in Experiment 1 (Mouse 1 and Mouse 2). **(F)** Distribution of each sample based on genotype (WT versus inducible PD-1^{del.}) and PD-1 protein status in Experiment 2 (Mouse 3-6). Plots split based on whether cells were clas



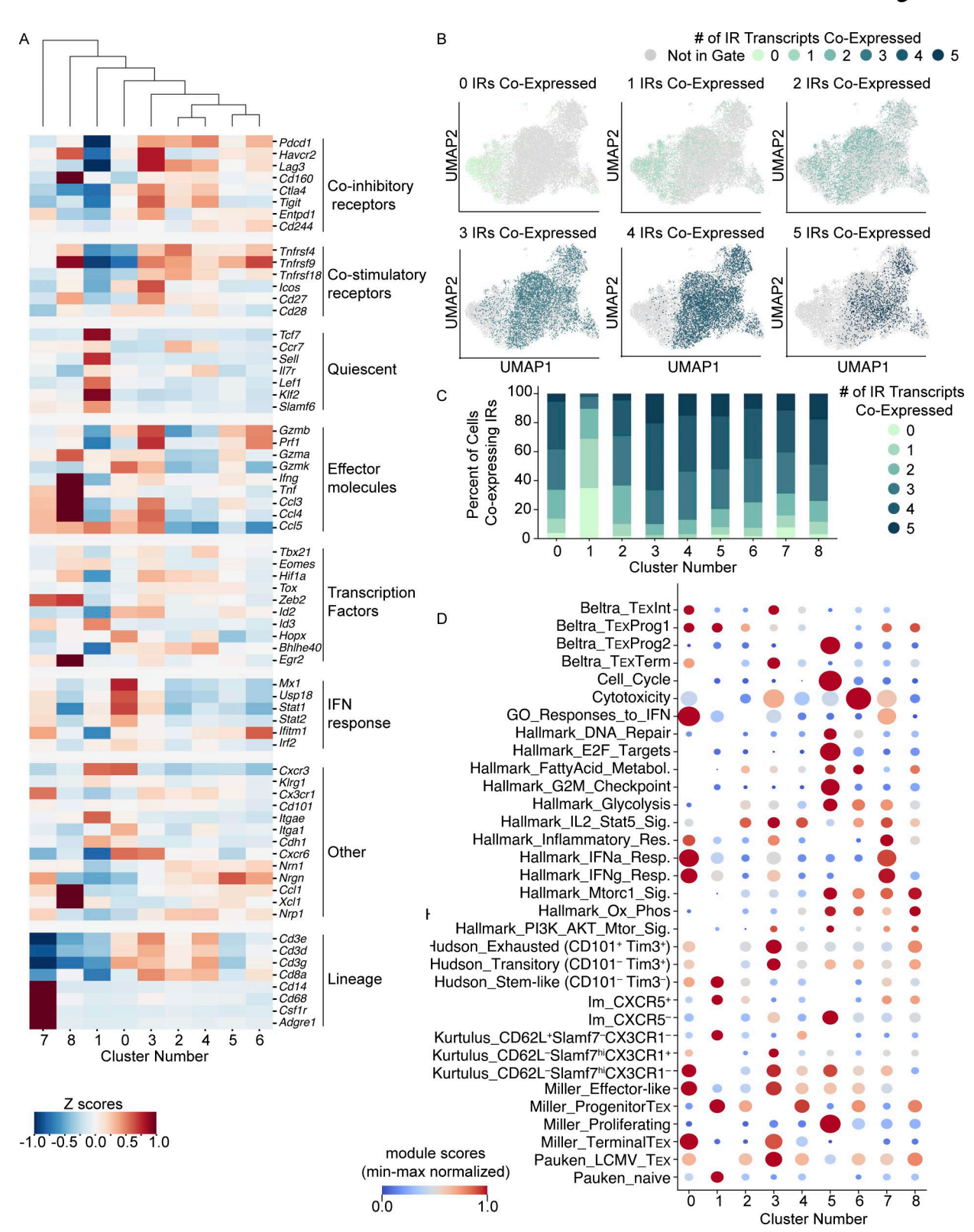


Figure S2. Expression of select transcripts, IR co-expression, and enrichment of key signatures in the scRNA-seq data from CD8* TILs from MC38 tumors. (A) Heat map showing Z scores of manually curated genes grouped by biological properties across the eight clusters shown in Fig. 3 B. (B) Co-expression analysis showing distribution of cells expressing 0, 1, 2, 3, 4, or 5 IRs based on transcript levels (transcripts included were *Havcr2*, *Lag3*, *Tigit*, *Cd160*, and *Ctla4*.) A cell was determined to be positive for each individual IR if it expressed any count greater than zero. (C) Quantification of IR transcript co-expression shown in B separated by cluster. (D) Enrichment of key gene signatures associated with exhausted CD8* T cell subsets and/or different biological properties (e.g., response to IFN, cell cycle, glycolysis, oxidative phosphorylation). Dot size is proportional to the min-max normalized expression values. Signatures used can be found in Table S2. For the plots in A–D, shown are all cells combined from two independent experiments, representing n = 4 mice per genotype.



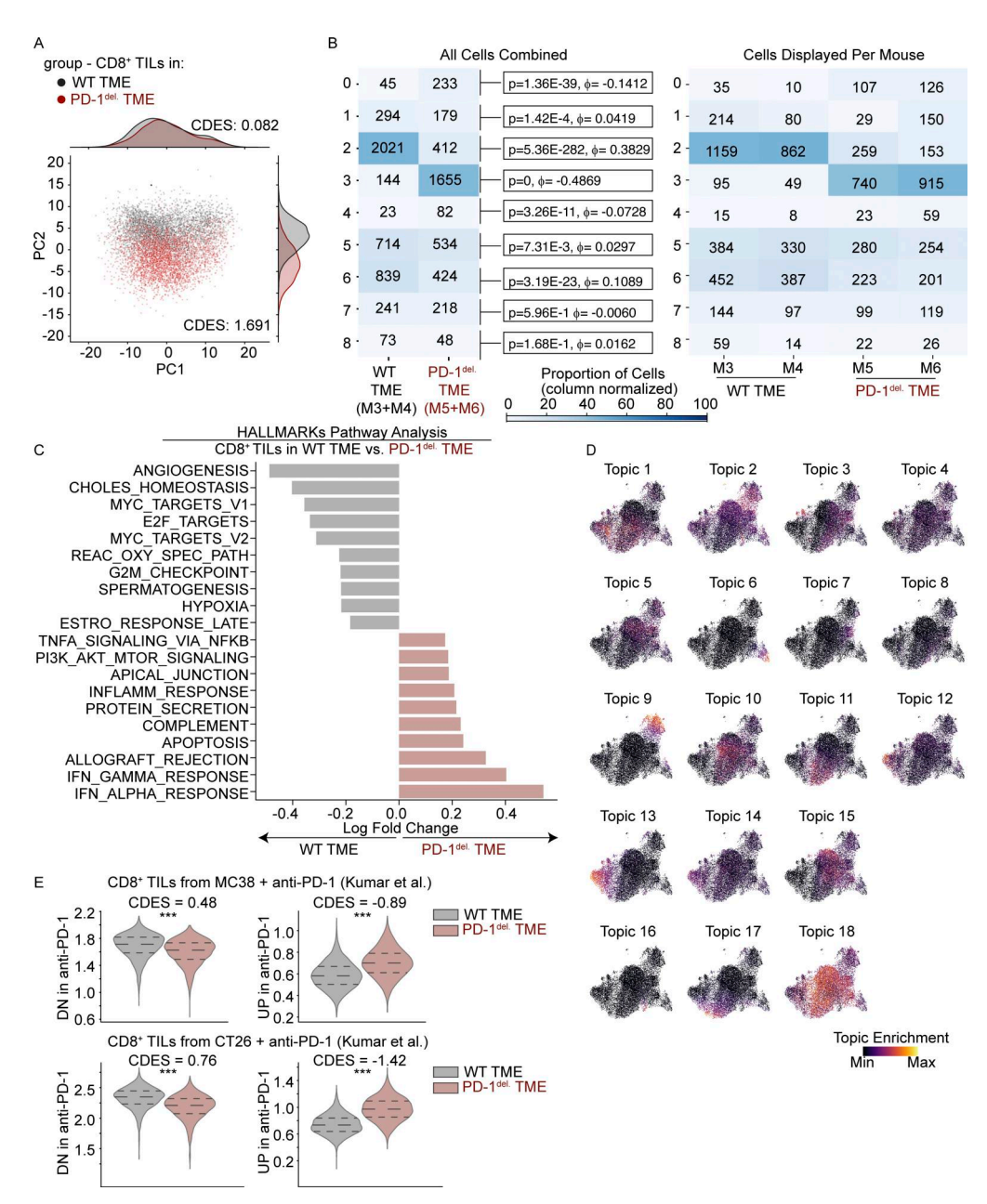


Figure S3. Transcriptional differences between total CD8⁺ TILs in WT versus inducible PD-1^{del} mice and comparison with changes in anti-PD-1treated mice. (A) Joint plot showing the first two principal components of gene expression and distribution of CD8+ TILs in the WT versus inducible PD-1^{del.} TME. Effect size (Cohen's D, referred to as CDES) between groups is indicated. PC1 CDES = 0.082; PC2 CDES = 1.691. (B) Heat map showing the proportion of cells in each cluster between CD8+ TILs in WT control and inducible PD-1^{del.} mice. Indicated are the raw cell counts (in the box), P values, and phi (\$\phi\$) coefficient (effect sizes) (next to the box). P values were calculated using Fisher's exact test. The color indicates the proportion of cells in each cluster, normalized by columns. On the left is a plot of all cells from experiment (Exp) 2 grouped based on genotype (WT versus inducible PD-1^{del.} mice, two mice per group). On the right is a plot of the cells from Exp 2 broken up by individual mouse, showing that the individual mice reproduce the pattern seen in the combined dataset. (C) GSEA of HALLMARK gene sets comparing CD8+ TILs in WT control and inducible PD-1^{del.} mice. Shown are only the top 10 significantly different gene sets between groups. Full names of each pathway, enrichment scores, and P values can be found in Table S4. (D) UMAPs of the topic weights for each topic. Full list of top 50 genes per topic can be found in Table S5. (E) Violin plots showing module scores in the scRNA-seq data generated from CD8+TILs from WT control and inducible PD-1^{del.} mice. Modules shown are signatures of upregulated and downregulated genes generated from scRNA-seq from CD8⁺ TILs from mice that received anti-PD-1 treatment. Modules derived from Kumar et al. (2022). (Top) Modules shown are differentially expressed genes from CD8⁺ TILs from mice with MC38 tumors treated with anti-PD-1 versus isotype control-treated mice (harvested at day 13). The left plot shows the module of genes downregulated in anti-PD-1-treated compared with isotype control (P = 7.22 × 10⁻¹⁰⁵; CDES = 0.48), and the right plot shows the module of genes upregulated in anti-PD-1treated compared with isotype control ($P = 6.99 \times 10^{-282}$, CDES = -0.89). (Bottom) Modules shown are differentially expressed genes from CD8+TILs from mice with CT26 tumors treated with anti-PD-1 versus isotype control-treated mice (harvested at day 17). The left plot shows the module of genes downregulated in anti-PD-1-treated mice compared with isotype control ($P = 6.06 \times 10^{-238}$, CDES = 0.76), and the right plot shows the module of genes upregulated in anti-PD-1treated mice compared with isotype control (P = 0; CDES = -1.42). P values were calculated using a two-sided Mann-Whitney U test. Plots in A-C and E include cells from one independent experiment, representing n = 2 mice per genotype. Plots in D include cells from two independent experiments, representing n = 4mice per genotype. Asterisks (***) indicate P < 0.0001. Exact P values listed in each panel.



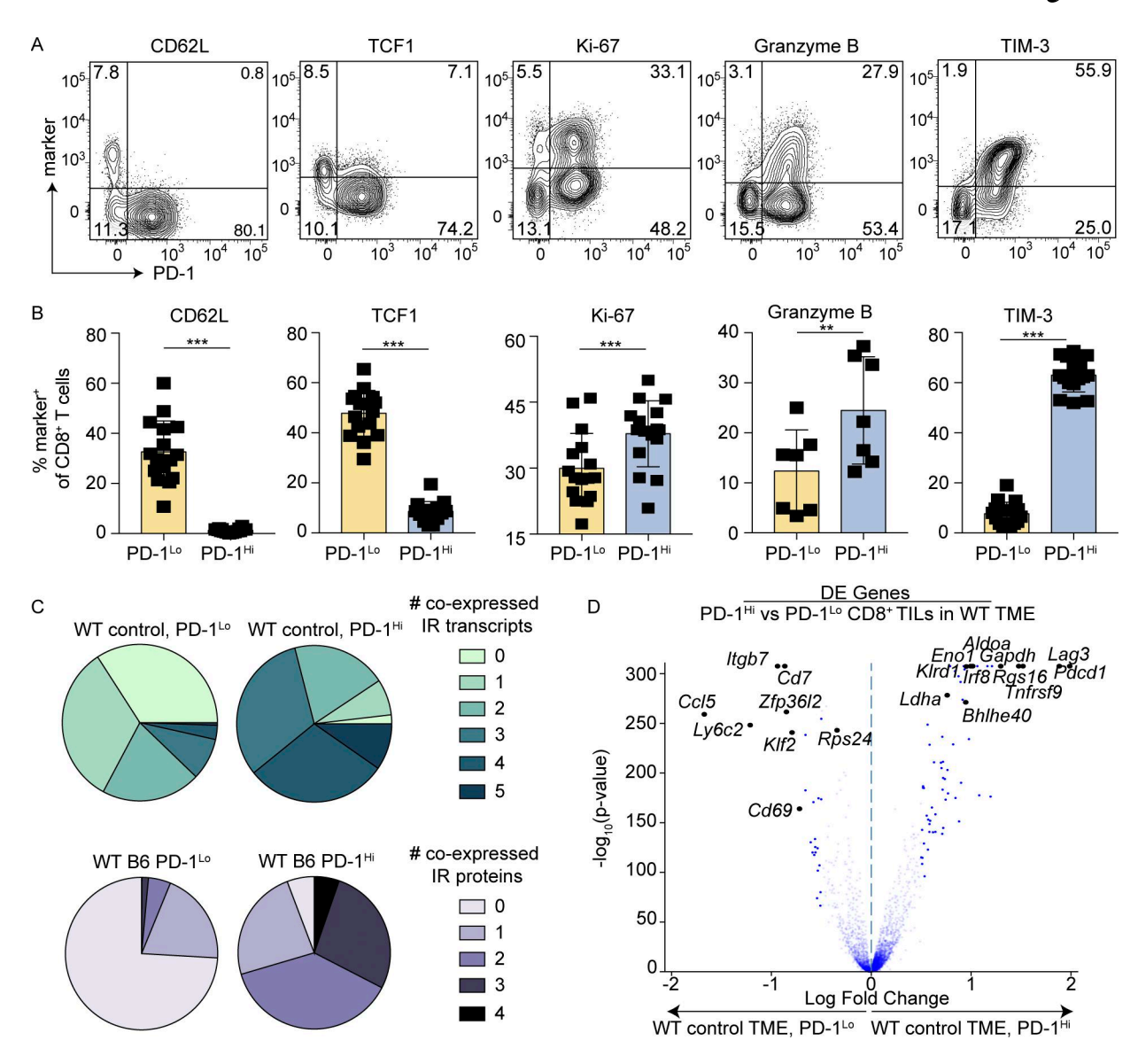


Figure S4. **PD-1^{Hi} and PD-1^{Lo} CD8* TILs are phenotypically, functionally, and transcriptionally distinct in MC38 tumors in WT control mice. (A)** Representative flow cytometry contour plots gated on CD8* T cells in MC38 tumors in WT C57BL/6 mice at day 21 after tumor cell implantation. Full gating strategy is size, singlets, live, CD45*, CD8* cells. PD-1 is shown on the x axis, and each individual marker shown on the y axis is indicated above the plot. **(B)** Quantification of the flow cytometry data shown in A, showing the percentage of PD-1^{Hi} or PD-1^{Lo} CD8* T cells expressing each indicated marker. Data are shown from three experiments combined for all markers except granzyme B, which is from two experiments combined. For all markers except granzyme B, n = 17 mice. For granzyme B, n = 7 mice. Significance was assessed using a paired t test. PD-1^{Lo} versus PD-1^{Hi}: CD62L, P < 0.0001***; TCF-1, P < 0.0001***; Ki-67, P < 0.0001***; granzyme B, P = 0.0015**; TIM-3, P < 0.0001***. **(C)** (Top) Quantification of IR transcript co-expression separated by sample (showing PD-1^{Li} and PD-1^{Lo} cells in WT control [UBC-CreERT2⁻ PD-1^{f/f}] mice), showing the frequency of CD8* TILs co-expressing the select number of IR transcripts (ranging from 0 to 5 IRs expressed/co-expressed). IR transcripts included in the analysis were *Havcr2* (encoding TIM-3), *Lag3* (encoding LAG-3), *Tigit* (encoding TIGIT), *Cd160* (encoding CD160), and *Ct1a4* (encoding CTLA-4). (Bottom) Pie charts of protein data (using flow cytometry) showing the frequency of PD-1^{Hi} or PD-1^{Lo} CD8* T cells co-expressing IR proteins from MC38 tumors in WT C57BL/6 mice. Flow cytometry data shown are from two experiments with *n* = 10 mice in total. IR proteins included were TIM-3, LAG-3, TIGIT, and CD160. **(D)** Volcano plot showing differentially expressed genes between PD-1^{Hi} and PD-1^{Lo} CD8* TILs in WT control (UBC-CreERT2⁻ PD-1^{f/f}) mice. Individual genes of interest are indicated on the plot. The entire list of differentially expressed g



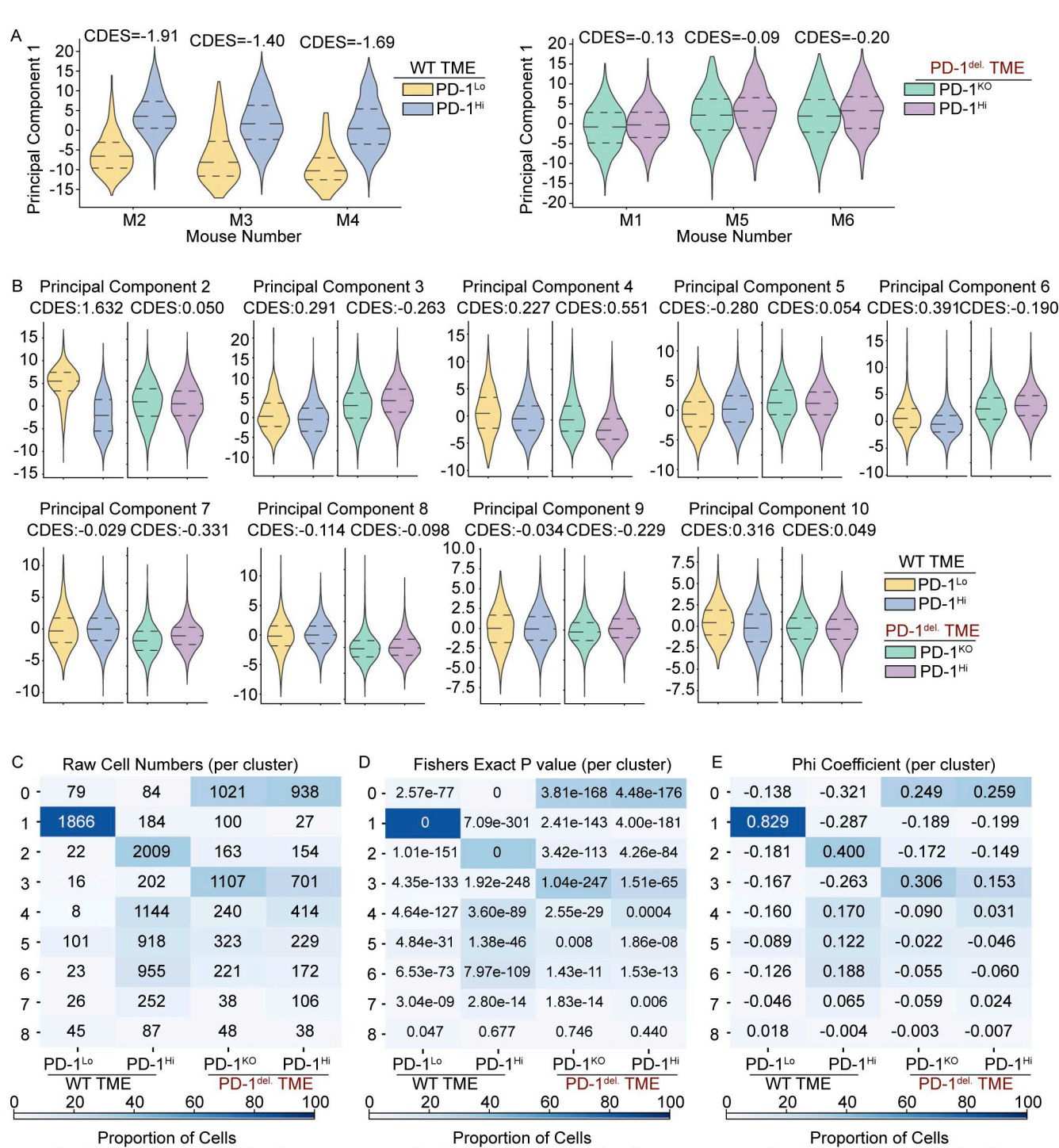


Figure S5. Quantification of principal components and cluster enrichments between PD-1^{Hi} and PD-1^{Lo} CD8⁺ TILs in WT mice and PD-1^{Hi} and PD-1^{KO} CD8⁺ TILs in inducible PD-1^{del}. mice. (A) Violin plots showing principal component 1 scores for each mouse individually for both experiment (Exp) 1 and Exp 2 (M2+M3+M4 = WT TME, M1+M5+M6 = inducible PD-1^{del} TME), split up by PD-1 status (PD-1^{Hi} versus PD-1^{Lo} in the WT TME, and PD-1^{KO} versus PD-1^{Hi} in the inducible PD-1^{del} TME). Shown are the CDES and Mann–Whitney P value for each mouse. In the WT TME, M2: P = 0 and CDES = -1.91; M3: P = 5.9 × 10⁻⁴⁸ and CDES = -1.40; M4: P = 1.4 × 10⁻³⁴ and CDES = -1.69. In the inducible PD-1^{del}. TME, M1: P = 0.00089 and CDES = -0.13; M5: P = 0.075 and CDES = -0.09; M6: P = 0.00032 and CDES = -0.20. (B) Violin plots showing the scores for principal components 2–10. Violins are colored by genotype and PD-1 status according to the Legend in the bottom right corner. Indicated above each pair within a genotype (e.g., PD-1^{Hi} versus PD-1^{Lo} or PD-1^{KO} versus PD-1^{Hi}) is the CDES. (C-E) Heat maps showing the proportion of cells in each cluster between CD8⁺ TILs in inducible PD-1^{del}. (PD-1^{KO} and PD-1^{Hi}) and WT control (PD-1^{Hi} and PD-1^{Lo}) mice. Values in each box indicated the raw cell counts (C), P values (D), and phi coefficient (E). Color indicates the proportion of cells in each cluster, normalized by columns. P values were calculated using Fisher's exact test. (A-E) includes all cells from Exp 1+2 (containing four mice in total per group) grouped based on the genotype (WT versus inducible PD-1^{del} mice).

(in cluster, column normalized)

(in cluster, column normalized)

(in cluster, column normalized)



Provided online are Table S1, Table S2, Table S3, Table S4, Table S5, Table S6, Table S7, Table S8, Table S9, Table S10, Table S11, and Table S12. Table S1 shows upregulated genes for each cluster in the CD8+T cell single-cell dataset from MC38 tumors from inducible PD-1^{del.} mice (e.g., UBC-CreERT2+ PD-1^{f/f} mice) versus WT control mice (e.g., UBC-CreERT2- PD-1^{f/f} mice). Table S2 shows gene signatures from or derived from the literature on exhausted CD8+ T cell subsets and/or different biological properties. Table S3 shows differentially expressed genes between CD8+ TILs from inducible PD-1^{del.} mice (e.g., UBC-CreERT2+ PD-1^{f/f} mice) versus WT control mice (e.g., UBC-CreERT2- PD-1^{f/f} mice) (Experiment [Exp] 2 only). Table S4 shows pathway analysis between CD8+ TILs from inducible PD-1^{del.} mice (e.g., UBC-CreERT2+ PD-1^{f/f} mice) versus WT control mice (e.g., UBC-CreERT2- PD-1^{f/f} mice) (Exp 2 only). Table S5 shows top 50 genes by weight for topic modeling (18 topic set) in MC38 tumors from inducible PD-1^{del.} mice (e.g., UBC-CreERT2+ PD-1f/f mice) versus WT control mice (e.g., UBC-CreERT2- PD-1f/f mice), as well as the corresponding weights for the genes in each topic. Table S6 shows comparison of differentially expressed genes between CD8+ TILs from mice with MC38 or CT26 tumors treated with anti-PD-1 (from Kumar et al. [2022]) and CD8+ TILs from inducible PD-1^{del.} mice versus control (from Exp 2 only). Table S7 shows common language effect sizes for the genes in CD8+ TILs from MC38 tumors in inducible PD-1^{del.} versus WT control mice compared with the posttreatment versus pretreatment comparison in select patient datasets. Table S8 shows differentially expressed genes between PD-1Hi and PD-1Lo CD8+ TILs in WT control mice (e.g., UBC-CreERT2- PD-1f/f mice). Table S9 shows differentially expressed genes between predicted PD-1^{Lo} but non-KO (e.g., PD-1^{Lo} Pdcd1^{WT}) and predicted PD-1^{KO} (e.g., PD-1^{Lo} Pdcd1^{KO}) CD8⁺ TILs in inducible PD-1^{del.} mice (e.g., UBC-CreERT2⁺ PD-1^{f/f} mice). Table S10 shows differentially expressed genes between PD-1^{HI} CD8⁺ TILs in WT control mice (e.g., UBC-CreERT2⁻ PD-1^{f/f} mice) and PD-1^{HI} CD8⁺ TILs in inducible PD-1^{del.} mice (e.g., UBC-CreERT2+ PD-1^{f/f} mice). Table S11 shows differentially expressed genes between PD-1^{Hi} and PD-1^{KO} CD8+ TILs in inducible PD-1^{del.} mice (e.g., UBC-CreERT2* PD-1^{f/f} mice). Table S12 shows housekeeping gene list used to filter cells in the single-cell dataset.